A rockslide-generated tsunami in a Greenland fjord rang Earth for 9 days

Kristian Svennevig, Stephen P. Hicks, Thomas Forbriger, Thomas Lecocq, Rudolf Widmer-Schnidrig, Anne Mangeney, Clément Hibert, Niels J. Korsgaard, Antoine Lucas, Claudio Satriano, et al.

Pre-print paper published in *Science* on 13 September 2024.
Published version: http://www.science.org/doi/10.1126/science.adm9247

A rockslide-generated tsunami in a Greenland fjord rang Earth for 9 days

Kristian Svennevig[1], Stephen P. Hicks[2], Thomas Forbriger[3], Thomas Lecocq[4], Rudolf Widmer-Schnidrig[5], Anne Mangeney[6], Clément Hibert[7], Niels J. Korsgaard[1], Antoine Lucas[6], Claudio Satriano[6], Robert E. Anthony[8], Aurélien Mordret[9,1], Sven Schippkus[10], Søren Rysgaard[11], Wieter Boone[12], Steven J. Gibbons[13], Kristen L. Cook[9], Sylfest Glimsdal[13], Finn Løvholt[13], Koen Van Noten[4], Jelle D. Assink[14], Alexis Marboeuf[6], Anthony Lomax[15], Kris Vanneste[4], Taka'aki Taira[16], Matteo Spagnolo[17], Raphael De Plaen[4], Paula Koelemeijer[18], Carl Ebeling[19], Andrea Cannata[20,21], William D. Harcourt[17], David G. Cornwell[17], Corentin Caudron[22,23], Piero Poli[24], Pascal Bernard[6], Eric Larose[9], Eleonore Stutzmann[6], Peter H. Voss[1], Bjorn Lund[25], Flavio Cannavo[21], Manuel J. Castro-Díaz[26], Esteban Chaves[27], Trine Dahl-Jensen[1], Nicolas De Pinho Dias[6], Aline Déprez[28], Roeland Develter[12], Douglas Dreger[16], Läslo G. Evers[14,29], Enrique D. Fernández-Nieto[30], Ana M.G. Ferreira[2], Gareth Funning[31], Alice-Agnes Gabriel[32,33], Marc Hendrickx[4], Alan L. Kafka[34], Marie Keiding[1], Jeffrey Kerby[11,35], Shfaqat A. Khan[36], Andreas Kjær Dideriksen[11], Oliver D. Lamb[37], Tine B. Larsen[1], Bradley Lipovsky[38], Ikha Magdalena[39], Jean-Philippe Malet[7,40], Mikkel Myrup[41], Luis Rivera[7], Eugenio Ruiz-Castillo[11], Selina Wetter[6], Bastien Wirtz[7].

Pre-print paper published in *Science* on 13 September 2024.
Published version: http://www.science.org/doi/10.1126/science.adm9247
1. Geological Survey of Denmark and Greenland, Denmark
2. Department of Earth Sciences, University College London, UK
3. Geophysical Institute, Karlsruhe Institute of Technology (KIT), Germany
4. Seismology - Gravimetry, Royal Observatory of Belgium, Brussels, Belgium
5. Institute of Geodesy, University of Stuttgart, Germany
6. Université Paris Cité, Institut de Physique du Globe de Paris, CNRS, Paris F-75005, France
7. Institut Terre et Environnement de Strasbourg (ITES), CNRS UMR 7063, Université de Strasbourg, Strasbourg, France
8. U.S. Geological Survey, Albuquerque, New Mexico, USA
9. Univ. Grenoble Alpes, Univ. Savoie Mont Blanc, CNRS, IRD, Univ. Gustave Eiffel, ISTerre, 38000 Grenoble, France
10. Institute of Geophysics, Centre for Earth System Research and Sustainability (CEN), Universität Hamburg, Hamburg, Germany
11. Department of Biology, Arctic Research Centre, Aarhus University, Denmark
12. Flanders Marine Institute, Belgium
13. Norges Geotekniske Institutt, Norway
14. Royal Netherlands Meteorological Institute (KNMI), Netherlands
15. ALomax Scientific, Mouans Sartoux, France
16. Berkeley Seismological Laboratory, University of California Berkeley, USA
17. School of Geosciences, University of Aberdeen, UK
18. Department of Earth Sciences, University of Oxford, UK
19. Institute of Geophysics and Planetary Physics, University of California San Diego, USA
20. Università di Catania, Dipartimento di Scienze Biologiche, Geologiche e Ambientali – Sezione di Scienze della Terra, Italy
21. Istituto Nazionale di Geofisica e Vulcanologia, Osservatorio Etneo – Sezione di Catania, Catania, Italy
22. Université libre de Bruxelles, Belgium
23. Wel Research Institute, Belgium
24. University of Padova, Italy
25. Department of Earth Sciences, Uppsala University, Sweden
26. University of Malaga, Spain
27. Volcanological and Seismological Observatory of Costa Rica, OVSICORI-UNA, Costa Rica
28. Data-Terra / Theia, CNRS UAR 2013, Strasbourg, France
29. Delft University of Technology, Netherlands
30. University of Sevilla, Spain
31. University of California, Riverside, USA
32. Scripps Institution of Oceanography, University of California San Diego, La Jolla, USA
33. Ludwig-Maximilians-Universität München, Munich, Germany
34. Weston Observatory, Boston College, USA
35. Scott Polar Research Institute, Department of Geography, University of Cambridge, Cambridge, UK
36. DTU Space, Technical University of Denmark, Denmark
37. GNS Science | Te Pū Ao, Wairakei Research Centre, 114 Karetoto Road, RD4, Taupō 3384, New Zealand, New Zealand
38. University of Washington, Seattle, USA
39. Institut Teknologi Bandung, Bandung, Indonesia
40. Data-Terra / ForM@Ter, CNRS UAR 2013, Strasbourg, France
41. Greenland National Museum & Archives, Greenland

*Corresponding author. Email: ksv@geus.dk

Pre-print paper published in *Science* on 13 September 2024.
Published version: http://www.science.org/doi/10.1126/science.adm9247

One-sentence summary

A 25 × 10^6 m^3 rockslide in East Greenland triggered a 9-day seiche leading to a rare 10.88 mHz monochromatic global seismic signal.

Abstract

Climate change is increasingly predisposing polar regions to large landslides. Tsunamigenic landslides have occurred recently in Greenland (Kalaallit Nunaat), but none have been reported from the eastern fjords. In September 2023, we detected the start of a 9-day-long, global 10.88-millihertz (92-second) monochromatic very-long-period (VLP) seismic signal, originating from East Greenland. We demonstrated how this event started with a glacial thinning induced rock-ice avalanche of 25 × 10^6 cubic meters, plunging into Dickson Fjord, triggering a 200 m high tsunami. Simulations show the tsunami stabilized into a 7-meter-high long-duration seiche with a frequency (11.45 mHz) and slow amplitude decay that were nearly identical to the seismic signal. An oscillating, fjord-transverse single force with a maximum amplitude of 5 × 10^{11} newtons reproduced the seismic amplitudes and their radiation pattern relative to the fjord, demonstrating how a seiche directly caused the 9-day-long seismic signal. Our findings highlight how climate change is causing cascading, hazardous feedbacks between the cryosphere, hydrosphere, and lithosphere.

Pre-print paper published in *Science* on 13 September 2024.
Published version: http://www.science.org/doi/10.1126/science.adm9247

Steep slopes are prone to destructive landslides that are increasingly likely to occur because of climate change (*1*). In cold regions, this increase may be driven by glacial debuttressing, permafrost degradation, or changes in precipitation (*2–5*). A landslide impacting a confined water body, such as a fjord, may produce a destructive tsunami (*6–9*), as demonstrated by previously reported events around the globe (e.g., Chile, Alaska, Norway, and Canada) (*8*, *10–13*). Similar events have occurred recently in Greenland (*Kalaallit Nunaat*) (*14–17*), as exemplified by the 2017 Karrat Fjord event along the west coast (Fig. 1), which caused four fatalities and left two villages permanently abandoned (*17*). However, no such events have previously been observed in East Greenland.

Large landslides are effective sources of long-period (> 20 s) seismic radiation owing to their typical long durations (~10 to 100 s), allowing their dynamics to be probed remotely with seismic data (*18–20*). The tsunamis induced by such landslides may also produce characteristic seismic signatures, especially in the near field (*21*, *22*). In closed and semi-enclosed basins, such tsunamis occasionally set up standing waves called seiches (*23–25*), in which water sloshes back and forth at a specific resonant frequency. Because their oscillation frequency derives from basin eigenmodes, seiches offer distinctive long-period, monochromatic sources that can be used to remotely investigate energy transfer from the hydrosphere to the solid Earth. Yet so far, only short-duration (<1 hour) loading-induced tilt caused by seiches has been observed on very local (<30 km distance) seismometers (*24*, *26–28*). Signals have not been previously recorded at larger distances, and tsunami-induced seiches have not been modeled numerically. Therefore, quantifying how tsunamis and seiches dissipate and radiate elastic waves into the lithosphere remains an open issue further hampered by the lack of high-rate water level recordings of such events in confined water bodies.

On 16 September 2023, we observed an enigmatic very long-period (VLP) seismic signal propagating around the globe (Fig. 1A; fig. S1). Unlike broadband earthquake signals, the VLP signal was monochromatic, with a dominant frequency of 10.88 mHz (92 s period), lasting for up to 9 days. Our initial estimates of its source position centered on East Greenland (Fig. 1B); (*29*). At the same time, Greenlandic and Danish authorities received reports of a large tsunami at the (then unoccupied) Nanok station and research base at Ella Ø (*Ella Island*) (Fig. 1C). As an interdisciplinary and international research team, we have integrated local observations, multiscale imagery, regional-to-global scale seismic data, and landslide-tsunami simulations to present a detailed reconstruction of the first documented large, tsunamigenic landslide from East Greenland and how it generated global VLP seismic signal. A high-resolution bathymetry dataset (15 m spacing) in the Dickson Fjord area (fig. S2); (*29*) provided the basis for fine-scale modeling that yields insights into the generation and unusual dynamics of the tsunami.

Field and satellite observations of the landslide

On 16 September 2023 at 12:35 UTC (11:35 local East Greenland time), a 25×10^6 m^3 rockslide (*29*); (text S1) occurred on a mountain peak at Hvide Støvhorn 1200 m above Dickson Fjord (Fig. 2A-B; 72.81°N, 26.95°W; text S2). A large body of metamorphic rock (up to 150 m thick, 480 m wide, 600 m long) dropped westwards along a foliation-parallel failure plane dipping 45° (Fig. 2D-F; text S3). The rockslide impacted and shattered a 200 m-wide outlet glacier in a gully at 600-900 m elevation, then turned northward and moved down the 30-40° steep glaciated gully as a rock-ice avalanche (text S1), entraining ~2.2×10^6 m^3 of the uppermost ~13 m of the glacier (Fig. 2G); (*29*). An 80 x 220 m peninsula that supported the glacier's calving front disappeared (Fig. 2B, 3A), indicating that the rock-ice avalanche may have triggered a submarine landslide in a sediment cone deposited at the terminus of the gully glacier. On the basis of the fjord morphology from available elevation models (fig. S2);

Pre-print paper published in *Science* on 13 September 2024.
Published version: http://www.science.org/doi/10.1126/science.adm9247

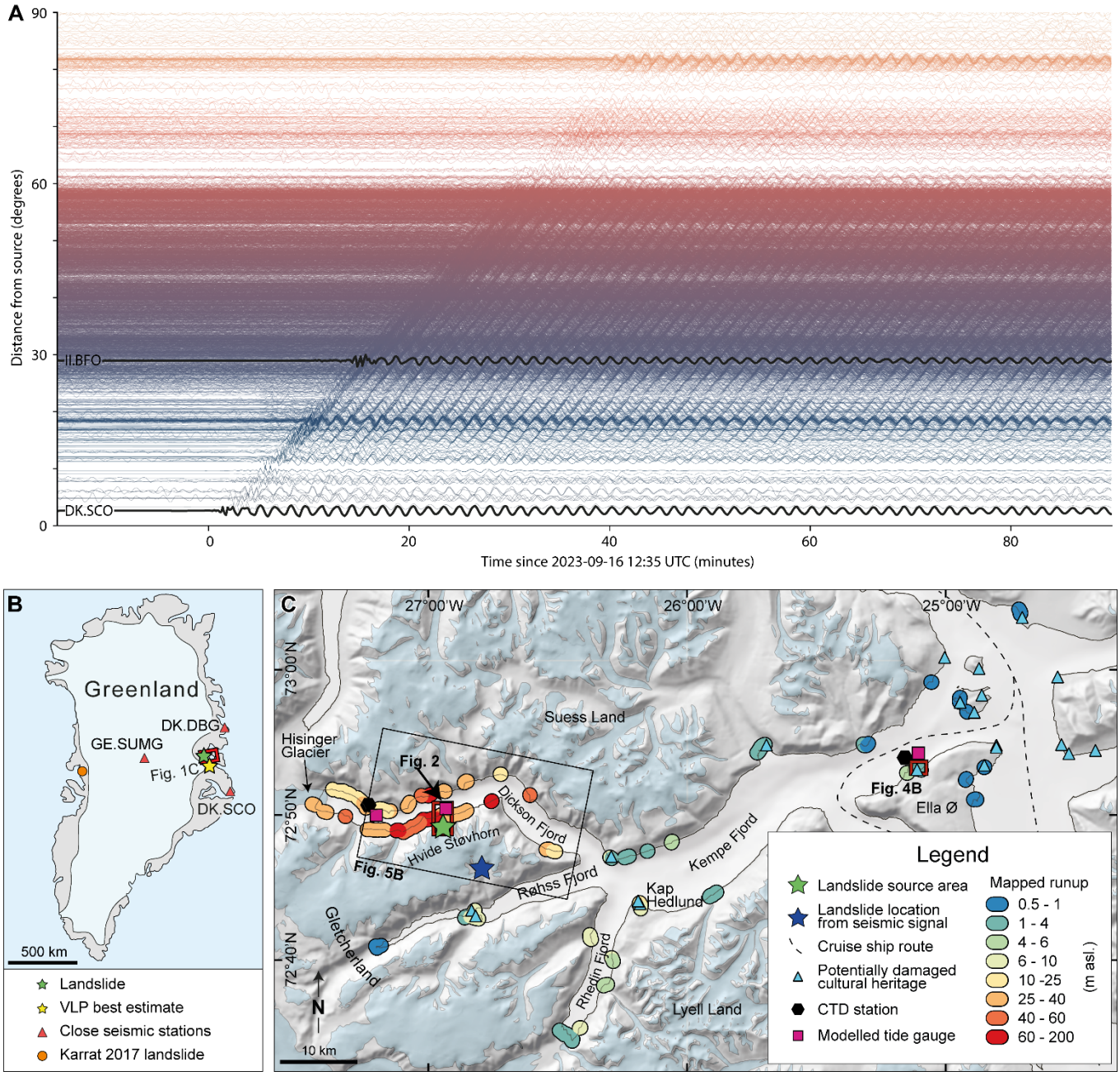

Fig. 1: Seismic signal, position, and local setting. ***(A)*** *Record section showing vertical-component waveforms from ~4,500 seismic stations up to 90° (10,000 km) from Dickson Fjord, with data bandpass filtered at 25-115 s, and waveforms colored by epicentral distance. These Rayleigh waves move-out with a phase velocity of 4.1 km/s. Stations DK.SCO and II.BFO are highlighted, with detailed views of their waveforms shown in Fig. 5C-D. Fig. S1 shows a similar, but global-scale, record section. (B) Overview map showing the closest seismic stations, the location of the landslide, and the very long-period (VLP) seismic source position using waveform back-projection (29).* ***(C)*** *Map of the Dickson Fjord area showing tsunami runup heights and the location of the landslide inferred from both satellite imagery and seismic data. CTD = conductivity, temperature and depth sensor.*

(*29*), we estimate a minimum total rock-ice avalanche run-out distance of 2.2 km.

The lower part of the rockslide failure plane extends beneath the pre-slide surface of the glacier (Figs. 2F-G), which had been thinning over the past decades (Fig. 2C); (*29*). We propose that this thinning led to debuttressing of the lower part of the unstable slope, triggering the rockslide. Such dynamic preconditioning is reported for other high-latitude and alpine landslides (*30*, *31*).

In addition to the 16 September 2023 event, we found evidence in satellite imagery of at least four smaller previous landslides and a subsequent one from the same gully (text S4; Table S1).

Landslide dynamics from seismic inversion

The 16 September 2023 landslide-tsunami event generated substantial seismic ground motions. At nearby stations (e.g., DK.SCO - 300 km away; Fig. 1B), we observed an emergent 200 s duration high-frequency (HF) (2-10 Hz) arrival with an extended coda, accompanied by a 60 s duration signal at lower frequencies (LF; 17-100 mHz). The 10.88 mHz VLP signal emerges from these higher-frequency signals (Fig. 3B).

The cigar-shaped HF signal contains two wavetrains. The first signal corresponds to the initial rockslide and the second to the rock-ice avalanche moving down the glacial tongue and entering Dickson Fjord. These waveform characteristics are typical of landslides (*20*), particularly those involving glacial ice entrainment (*18*, *20*, *32*), topographic obstacles, and water bodies (*33–35*). The LF waves come from acceleration and deceleration of the bulk mass on the Earth's surface, whereas the HF waves come from interactions between grains in the moving mass with the substrate (*20*, *36*). We used different methods (arrival time inversion, centroid moment tensor waveform inversion, cross-correlation) to show that the source, which originated at 16 September 2023 12:35:03 UTC, is consistent with the imagery-derived landslide location, with most computed positions within 20 km distance (fig. S3 & table S2). The landslide was sufficiently energetic to produce acoustic signals recorded on International Monitoring System (IMS) infrasound arrays up to 3,310 km away (I37NO, I43RU); (*29*).

To estimate the trajectory of the force imparted by the landslide on the Earth's surface, we inverted waveforms from the three closest seismic stations (Fig. 1B), bandpass filtered between 17 and 100 mHz, (*18–21*) (Fig. 3B); (*29*). Our inversion yields a maximum force of 192×10^9 N, corresponding to a mass of approximately 78-103 $\times$ 10^9 kg, equivalent to a volume of 29-38 $\times$ 10^6 m^3 (assuming a density of 2.70 g cm^{-3}); (*19*, *21*). From the fjord morphology, we estimate a total run-out distance of 2.2 km. Based on this assumption, the kinematic quantities derived from the inverted force give a 55×10^9 kg mass (~20×10^6 m^3), which is consistent with the structure from motion volume reconstruction (*29*). The rock-ice avalanche had a peak acceleration of 3.5 m s^{-2} at 42 s and a peak velocity of 47 m s^{-1} at 52 s after it initiated (Fig. 3D). We find two sudden, mid-path acceleration drops along the direction of movement before the final one ("D1" and "D2" in Fig. 3D), the first coinciding with the maximum of the upward vertical force and both with drops in the north force (Fig. 3C). D1 coincides with an amplitude peak in the HF signal, and D2 marks the onset of the second phase of the HF signal (Fig. 3B), showing the influence of topography (*34*). D1 is likely associated with the mass impacting the west wall; D2 likely corresponds to the moment when the front of the rock-ice avalanche reached the water, causing a deceleration to the overall center ofmass. Overall, the seismically inverted run-out path matches that inferred from imagery (Fig. 3A).

According to our inversion results and morphological observations, the higher frequency (>25 mHz) seismic waveforms clearly come from the rock-ice avalanche. However, the VLP component of the signal, which emerges.

Pre-print paper published in *Science* on 13 September 2024.
Published version: http://www.science.org/doi/10.1126/science.adm9247

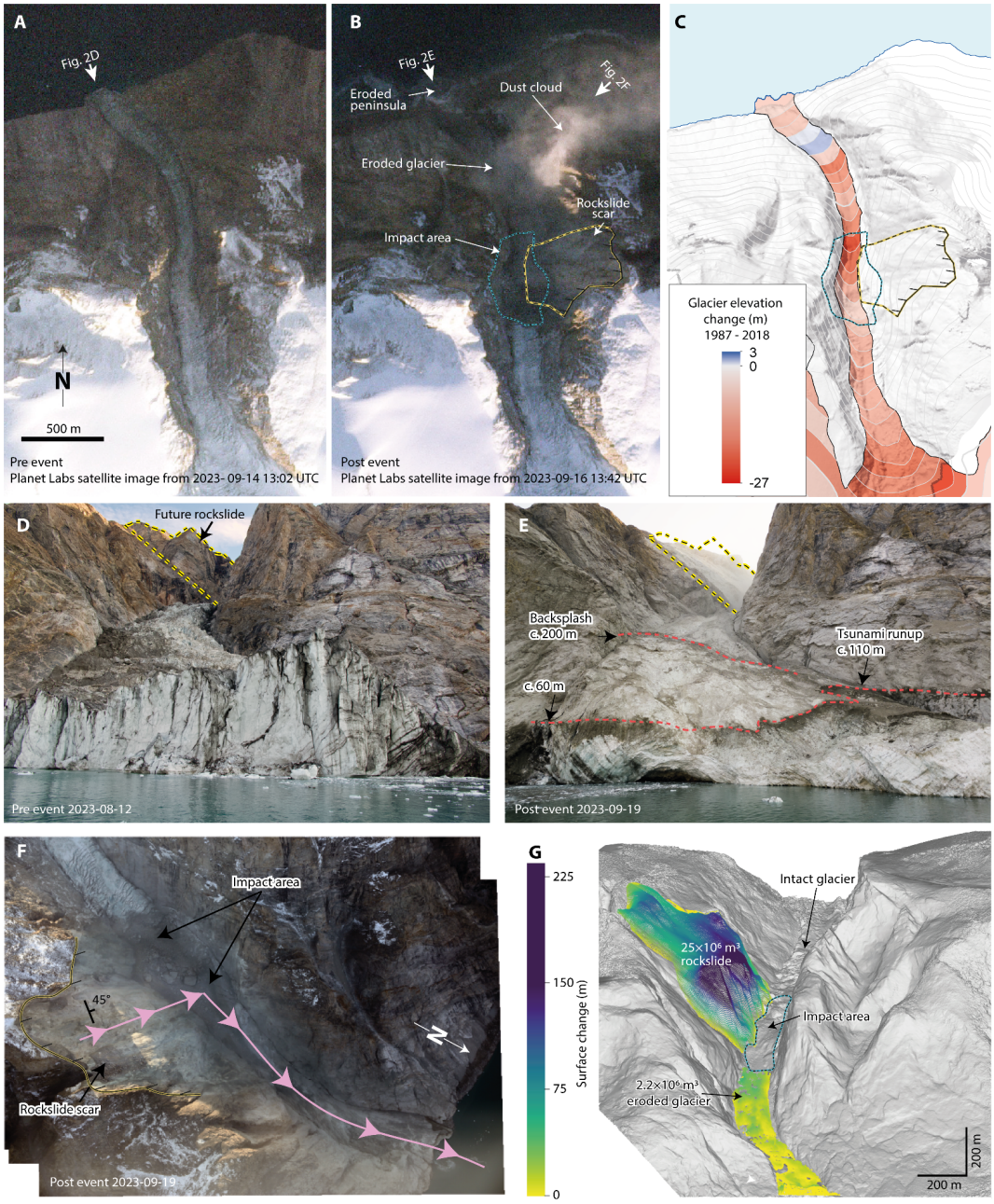

Fig 2. Landslide observations. *(A) Pre- and (B) post-event Planet Labs satellite image (locations in Fig. 1C). Image © 2023 Planet Labs PBC. (C) Mean elevation change during 1985-2018 of the glacier surface per 50 m elevation interval. Scale and field of view are the same for A,B,C. (D,E) Pre- and post-event field photos of the coastal slope (looking south, refer to arrows in A and B). The stippled yellow line outlines the rockslide source area. Location shown in A and B. Tsunami runup heights are indicated with stippled red lines on (E). (source of E: Sirius Dog Sled Patrol of the Joint Arctic Command). (F) Post-event aerial photomosaic from 19 September 2023 of the onshore landslide-affected area (location in B) (source: Joint Arctic Command of the Danish Navy). (G) Orthogonal projection (southward view) of the Structure from Motion point cloud (29), showing the failed bedrock volume and the entrained volume of the glacier below the impact area (stippled blue outline).*

Pre-print paper published in *Science* on 13 September 2024.
Published version: http://www.science.org/doi/10.1126/science.adm9247

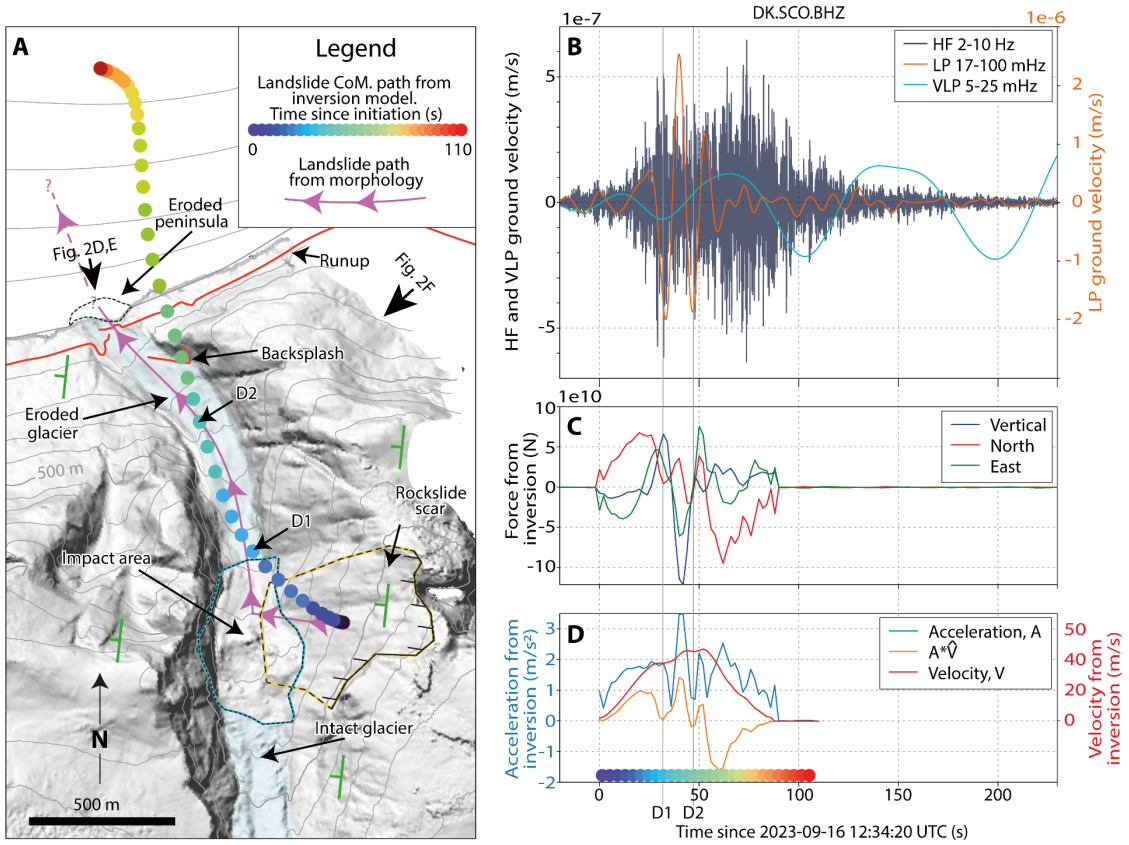

Fig. 3: Landslide seismic signal and modeling. *(A) Geomorphological map showing the landslide center-of-mass (CoM) runout paths from morphological interpretation and seismic inversion. Green symbols indicate the strike and dip direction of the foliation. (B) The seismic signal recorded at DK.SCO.BHZ (313 km distance), shifted by the travel time between the source location and the station (at 3 km/s velocity), with different bandpass filters applied. (C) The seismically inverted force of the landslide CoM acting on the Earth; (D) Modulus of the seismically-inverted acceleration (blue), velocity (red) and scalar product of the acceleration and the normalized velocity ($\hat{v}$; orange) of the CoM of the moving mass; D1 and D2 indicate the two first peaks of deceleration and are shown on the map in (A). The colorbar is the same as shown in (A).*

out of the higher-frequency waveforms (Fig. 3B), remains unexplained

Tsunami recordings and modeling

The impact of the 16 September 2023 rock-ice avalanche into the 540 m deep and 2.7 km wide Dickson Fjord triggered a tsunami with an initial backsplash with a runup height of ~200 m and subsequent waves up to 110 m high (Fig. 2E); (*29*). The tsunamigenic potential of the rock-ice avalanche was enhanced by its channelization into the gully, the entrainment of ice into the mobilized volume (*18*, *37*), and the glacier lowering the basal friction (*18*, *32*, *35*). At the Nanok station and research base at Ella Ø, 72 km away out-fjord, the tsunami had a local runup height of 4 m, inundating up to 80 m inland, and destroying infrastructure valued at nearly 200,000 USD (Fig. 1C, 4A-B). Elsewhere in the fjord system, near-coastal cultural heritage sites, such as Thule Culture Inuit archaeological sites and 20th-century trapper huts were well within the inundation reach and were assumed to be destroyed. The observed destruction of an old trapper hut at Kap Hedlund (Fig. 1C), which had never been affected

by tsunamis during its century-old history, demonstrates the unexpected size of the September 2023 event (text S5). Cruise ships pass east and west of Ella Ø every week in the ice-free season (Fig. 1C), but none were in the fjords during the tsunami.

The tsunami was recorded by nearby pressure sensors and sea level gauges (*29*, *38*) (Fig. 1C; fig. S18); (*29*). Out-fjord, at Ella Ø, a high turbidity signal was detected due to local sediment resuspension by the tsunami, peaking 3 hours after the initial tsunami and lasting 6-7 hours (Fig. 4C). The sea level gauge in Dickson Fjord, located 8 km west of the landslide impact point along the shoreline, recorded a maximum peak-to-peak amplitude anomaly of ~0.4 m; however, its 15-minute sample interval almost certainly aliases out higher amplitudes (Fig. 4D).

We therefore relied on numerical modeling, validated by observed runup heights, to better understand the shorter-period component of the tsunami. We first modeled the tsunami using a linear dispersive Boussinesq model nested with a nonlinear shallow water inundation model (*GloBouss* algorithm); (*29*), to simulate the observed inundation, runup height, and the sea level gauge recording at Ella Ø (adding 0.7 m high-water spring tide at the time of the landslide). The simulated and observed runup heights compare well (Fig. 4A-B). To verify this result and to better simulate the longer-term evolution of the tsunami within Dickson Fjord we also used an independent, nonlinear hydrostatic model (*39*) that describes the rock-ice avalanche as a granular flow (*9*) (HySEA model); (*29*). However, modeling the long-term energy dissipation of tsunamis is a non-trivial task. Unrealistic, artificial damping due to numerical dissipation in complex bathymetric models is inherent in HySEA's finite-volume modeling scheme (*39–41*), thus masking realistic physical damping effects, such as out-fjord dissipation and bottom-friction. We indeed observed that numerical dissipation in the finite-volume model masks the effects of bottom friction for grid spacings of >7.5 m, with reduced dissipation in finer grids (fig. S5). This overall result is independently corroborated by GloBouss simulations (text S6). For our preferred simulation, we therefore used the most computationally feasible, finest grid spacing of 3 m, with a Manning bottom-friction parameter of 0.03 typically used in tsunami modeling (*41–43*).

Our preferred simulation set-up shows that at ~5 minutes after the material entered the water, the waves stabilize into a slowly decaying seiche with a maximum amplitude of 7.4 m and a dominant frequency of 11.45 mHz (87 s); (Figs. 4E, 5B & 5E; movies S1-S2). This eigenfrequency is directly related to the width and depth of Dickson Fjord, as shown in the analytical solutions (*42*).

Character of the VLP seismic signal

From the higher-frequency rock-ice avalanche signal (Fig. 3B), a prominent harmonic (monochromatic) signal emerges, with a frequency of 10.88 mHz (92 s), that is observed on seismometers and superconducting gravimeters globally for up to 9 days (Figs. 1A, 5, S6). The amplitude decay of this VLP signal is extremely slow (Fig. 5C). We quantify this decay by modeling the signal's envelope as $\exp\left(-\frac{t}{T}\frac{\pi}{Q}\right)$, where Q is the quality factor of a harmonic oscillator and T is its dominant period of 92 s (*29*). The initial Q of the signal is ~500, gradually increasing, to and stabilizing at, ~3,000 (Fig. 5C), indicating a non-exponential amplitude decay. The signal is phase-coherent and undergoes a 540 parts per million semidiurnal frequency modulation for at least its first 50 hours (fig. S7); (*29*).

Our back-projection analysis of global surface waves and regional waveform inversion using a resonating source-

time function with an equivalent moment magnitude of 5, finds a source location that is stable for 9 days originating from East Greenland near Dickson Fjord (Fig. 1B; table S2; movie S3); (*29*). However, the long wavelengths at such long periods (~400 km) limit the spatial resolution of these locations. Nevertheless, given that the VLP signal emerges in the coda of the HF signal (Figs. 3B, 5D), we assume it originates near the seismically derived landslide source position from HF waveforms (table S2). However, a landslide lasting several minutes could not have directly generated such a long duration, slowly decaying, highly monochromatic signal.

Instead, our analysis of three-component seismic waveforms from stations at teleseismic distances shows that the signal's radiation pattern directly relates to the water body in the fjord. We observed predominant Love wave radiation along the longitudinal axis of Dickson Fjord (070°) and Rayleigh wave radiation perpendicular to it (160°; Fig. 5A-B); (*29*). This pattern mimics the vertical-component signal duration (fig. S8), showing how the VLP signal's observed duration of up to 9 days depends on station azimuth relative to radiation pattern and site-dependent noise level.

Three weeks later, on 2023-10-11, a similar signal that originated from the same location, and showed the same fundamental period and radiation pattern, but with half the amplitude, was also observed globally. The signal was also associated with a landslide-tsunami event originating from the same gully with around half the vertical tsunami runup (text S4). A systematic search of past seismic data (1990-2023) and gravimeter data (1982-1994) from station II.ALE in northern Canada, revealed four additional smaller-amplitude, shorter-duration VLP signals with almost identical frequency (fig. S13). At least two of these events (February 2016 and January 2017) were associated with a rock-ice avalanche in the same gully, and, intriguingly, occurred when the fjord was ice-covered.

Although global seismic networks would have been sensitive enough to record them for at least three decades (*44*, *45*), similarly high-amplitude, globally observable, slowly decaying signals with a stable monochromatic period starting at the signal onset, are extremely rare. The handful of documented cases with dominant frequencies of >1 mHz have been related to volcanic activity, either through resonance excited by subsurface magmatism (*46*, *47*) or from explosive eruptions exciting the fundamental mode of Earth's atmosphere (~3.7 mHz) (*48*, *49*). In contrast, the Greenland VLP signals have a much slower decay and a different radiation pattern, making them different from previous observations.

A seiche as the source of the global VLP seismic signal

The VLP signal's radiation pattern and slow decay, compared with freely propagating Rayleigh waves, must be due to its source excitation because no high-Q Earth normal modes exist near 10.88 mHz (*50*). We thus propose that a freely decaying seiche oscillation in Dickson Fjord generated the observed VLP signals, for four reasons.

First, the numerical tsunami simulation stabilizes into a free seiche oscillation with a dominant frequency of 11.45 mHz (87 s period), which is very close to the 10.88 mHz frequency (92 s period) of the seismic signal (Fig. 5D-E). We attribute the small difference to unmodelled complexities in the fjord's bathymetry (*42*).

Second, the restoring force of the seiche acts in a direction perpendicular to Dickson Fjord and thus provides a horizontal transfer of momentum to the Earth's crust in that direction. This is consistent with the observed radiation pattern of Rayleigh- and Love-waves (Fig. 5A-B).

Pre-print paper published in *Science* on 13 September 2024.
Published version: http://www.science.org/doi/10.1126/science.adm9247

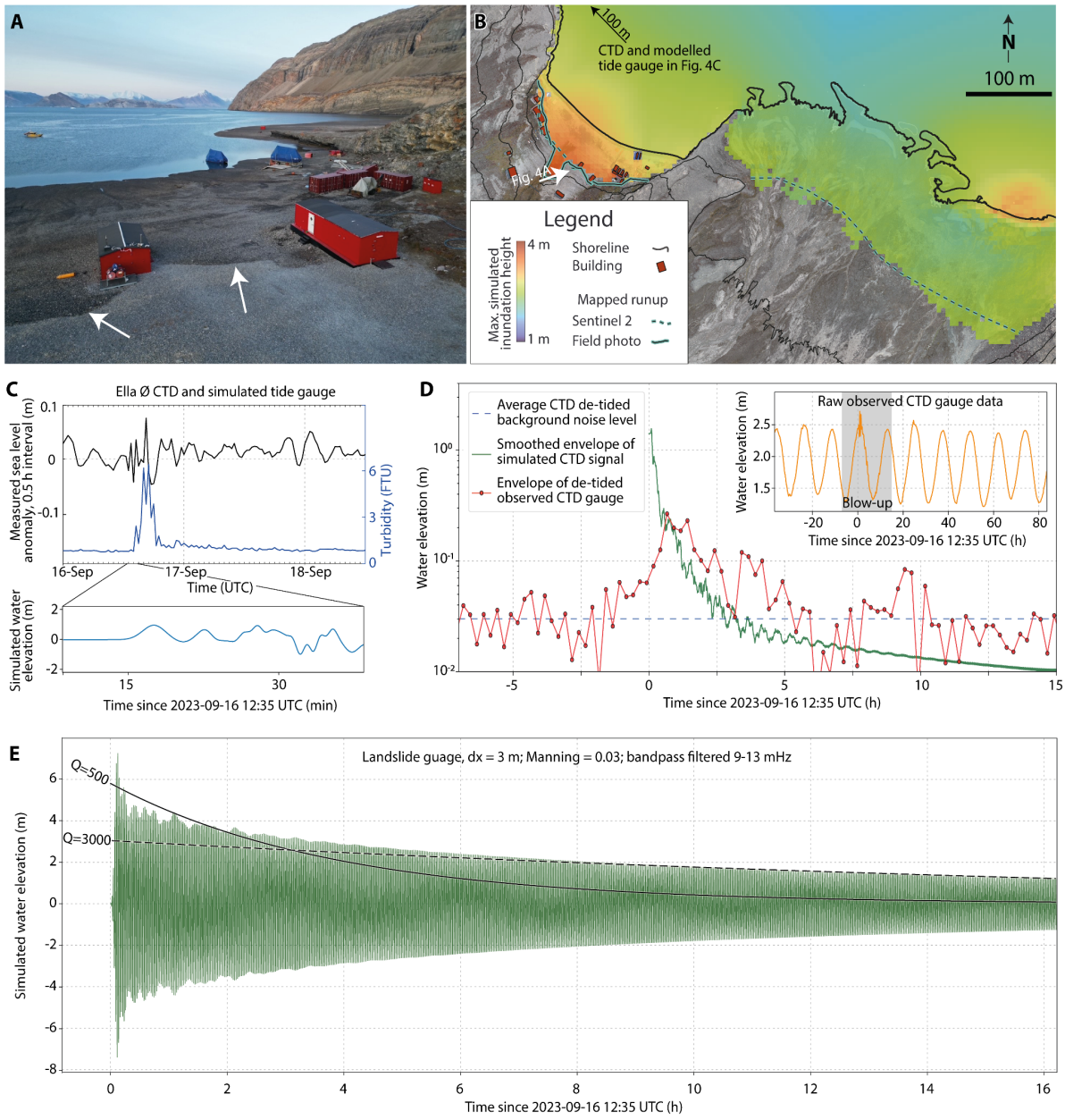

Fig. 4: Tsunami observations and modeling. ***(A)*** *Drone photo looking east-northeast showing the 4 m runup height at Ella Ø (white arrows). Source: Joint Arctic Command/Sirius of the Danish Navy.* ***(B)*** *Mapped and simulated tsunami runup at Ella Ø.* ***(C)*** *Observed and simulated tsunami at Ella Ø using the GloBouss tsunami model (43) (Fig. 1C). Upper panel: sea level and turbidity from the conductivity, temperature, and depth (CTD) station.* ***(D)*** *Comparison between observed (15-min sampling interval) and simulated (using the HySEA tsunami model) water level at the Dickson Fjord sea level gauge/CTD station (Fig. 1C & 5B).* ***(E)*** *Filtered (9 to 13 mHz bandpass) simulated long term tsunami water elevation at the landslide fjord impact location, with indicative exponential decay-rates labelled as Q-values. Its amplitude spectrum is shown in Fig. 5E.*

Pre-print paper published in *Science* on 13 September 2024.
Published version: http://www.science.org/doi/10.1126/science.adm9247

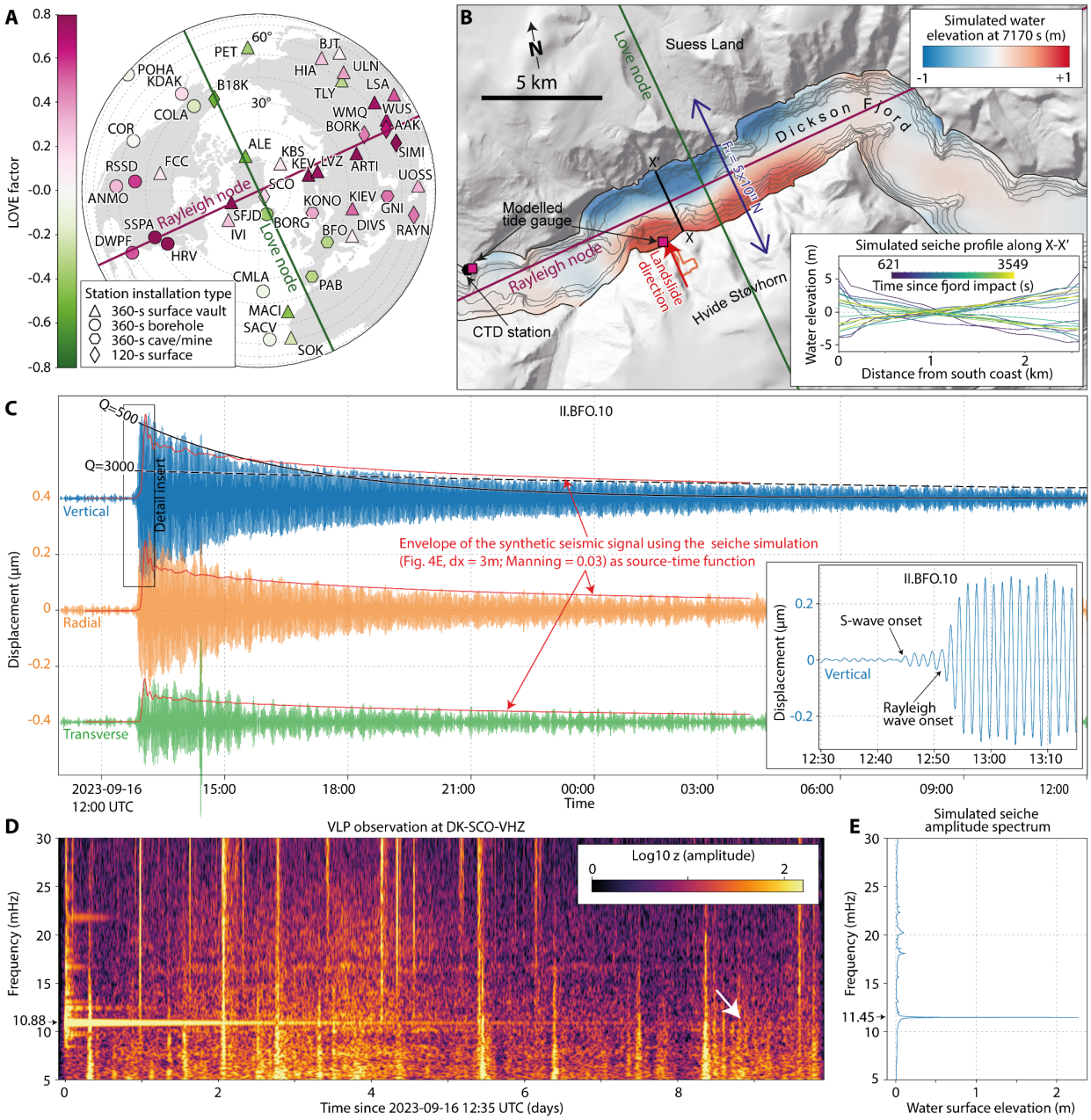

Fig. 5: Very long-period (VLP) seismic signal and comparison with simulated seiche. ***(A)*** *Locations of seismic stations with high-fidelity three-component VLP recordings, colored by dominant surface wave type (green = Rayleigh, pink = Love); (29). This radiation pattern matches the strike of Dickson Fjord and its perpendicular, as shown in* ***(B)****, where the background red-blue colors show a snapshot of the simulated seiche after 2 hours, along with the modeled direction of the oscillating horizontal single force (purple arrow). The inset shows the simulated seiche profile along X-X', at different timesteps.* ***(C)*** *Waveform recording from station II.BFO in Germany (29° away), showing dominant Rayleigh energy on the vertical and radial components, with weaker Love energy on the transverse. Indicative Q-values (black lines) highlight their slow, non-exponential decay. S-body waves arriving at 12:46 UTC (inset) carry the initial VLP signal. Synthetic seismogram envelopes (red lines) using the simulated seiche signal at the location of the landslide (Fig. 4E), scaled to a maximum horizontal force of 5 × 10^{11} N (29), match the maximum VLP amplitudes and their decay. All signals are 10- to 12 mHz bandpass filtered.* ***(D)***

*Vertical-component spectrogram from DK.SCO (2.6° away), showing the >9 day-long duration of the VLP signal (white arrow). (**E**) Amplitude spectrum of the simulated seiche time series at the landslide impact in the fjord (Fig. 4E).*

Fourth, the simulated free seiche oscillation shows a decay similar to that of the VLP signal. The seiche has a non-exponential decay, starting at a higher decay rate of $Q \sim 500$, and over a few hours, gradually transitions to a slower decay of $Q \sim 3000$ (Fig. 4E), matching very closely the decay of the VLP signal (Fig. 5C). Such a slowly dissipating seiche is predicted by two different modeling approaches, which are complementary and independent in terms of the physical processes involved and the numerical methods used. From our tsunami simulation with a fine grid spacing (i.e., 3 m, Manning 0.03), we use the near-landslide time series of the seiche (Fig. 4E) to generate a source-time function as input to the global seismic waveform modeling (*29*). The amplitudes, radiation pattern, and signal envelopes of the resulting synthetic seismograms are shown in Fig. 5C together with the recorded waveforms. The good match between synthetics and recordings corroborates the free seiche as the source of the VLP signal.

The freely decaying seiche oscillation in Dickson Fjord

Although a real-time conductivity, temperature, and depth (CTD) sensor (*29*) continuously measures water levels in the western part of Dickson Fjord (Figs. 1C & 5B), its telemetered sampling interval of 15 minutes strongly aliases the short-period tsunamis and the ~90 s period seiche (Fig. 4D). In addition, because the primary purpose of the CTD sensor located in the inner fjord was to detect calving events on the nearby Hisinger Glacier, our tsunami simulation hindcasts a much weaker seiche signal here, compared with the signal in the central segment of the fjord at the landslide (Fig. 5B; movie S2). Therefore, the seiche signal recorded by this CTD sensor would have fallen to pre-event noise levels after only ~5 hours (Fig. 4D). Thus, it is the distinctive combination of the tsunami simulation and seismic observations that corroborate the slowly decaying free seiche mechanism.

Although a previous study has reported earthquake tsunami-induced seiches persisting for several days in an island archipelago in the open ocean (*51*), the distinctively longer-duration and more slowly decaying VLP seismic signals documented in this study are likely related to the combination of a huge tsunami caused by a large fjord-transverse landslide and a highly confined water body in Dickson Fjord, with parallel shorelines. This effect is seen in the tsunami simulation, in which most seiche energy remains confined to the central segment of the fjord, with little leakage in- and out-fjord (Fig. 5B); (movie S2). The sharp bend in the inner fjord seems to prevent propagation of the resonant wave components to the outer fjord system. This barrier effect is supported by the two independent tsunami modeling approaches (text S6 in (*29*)). By contrast, the considerably more open fjord basins of Taan Fjord in Alaska and Karrat Fjord in West Greenland, with fjord-oblique slide directions, will have generated only weaker, shorter duration seiches, as recorded in the corresponding near-field (<30 km) seismic observations (*28*, *52*).

Landslide-tsunami-induced seiches must also have caused the five other, smaller VLP events. Two of these events were in winter, albeit with a slightly lower Q (table S1). Previous studies show that seiches can still occur in ice-covered water (*53*). During winter, the sea ice in the fjord is not completely fused to the coast, with a zone of tidal-induced fractures along the shore that can accommodate changing sea level with little energy dissipation (*54*).

The small deviation between the dominant frequency of the VLP (10.88 mHz) and simulated seiche (11.45 mHz) likely arises from uncertainties in the near-shoreline, shallow water bathymetry data (10% bathymetry difference

based on analytical solutions); (*42*). This effect is shown by our tsunami simulation results using coarser bathymetry dataset with 125 m spacing (*55*), which produced a larger, more discrepant dominant frequency of 12.45 mHz. Remaining minor differences between the decay rates of the observed VLP and synthetic waveforms could be attributed to unmodelled dissipation effects such as larger, high-amplitude waves breaking for the first cycles of the seiche (Figs. 4E, 5C), which are not well-modeled with our hydrostatic numerical simulation (*56*) non-linear frictional bottom-stress (*51*, *57*, *58*), and non-linear water-seismic coupling/transmission along the walls of the fjord. Lastly, we propose that an observed tidal modulation of the VLP signal (fig. S14) occurs because a wider channel during higher tides outstrips the weaker channel-deepening effect, as per analytic solutions (*42*), thus reducing the fjord's eigenfrequency and associated VLP frequency. However, uncertain bathymetry close to the shoreline at shallow depths again prevents a detailed reconstruction of this effect from our numerical model.

In this study, we have focused on the monochromatic, dominant frequencies in the observed VLP seismic signal and the tsunami simulation. However, away from these dominant frequencies, these signals contain a set of weaker, yet discernible spectral peaks (Fig. 5D-E), some of which are predicted overtones, whereas others are more enigmatic. For example, we identified a 90°-rotated radiation pattern in the first harmonic overtone compared with the fundamental. These weaker signals and their radiation patterns can be explored in more detail to further characterize this rare, unprecedented seiche event and to better understand how it transmits seismic energy into the solid Earth.

Conclusions and implications

Our study underscores intricate interconnections within the Earth system, specifically between the cryosphere, hydrosphere, and lithosphere. Our combined analyses, involving multiscale imagery, field data, tsunami simulations, and remote seismological data, demonstrate a complex, cascading chain of events in East Greenland. This sequence was originally preconditioned by climate change-induced glacial thinning, culminating, on 16 September 2023, in a large rockslide, which entered the fjord to generate a 200 m high tsunami. The tsunami evolved into an initially 7 m high, ~90 s period freely oscillating seiche that decayed slowly owing to the confined nature of the fjord and could be detected seismically for 9 days. The large tsunamigenic rock-ice avalanche is an extraordinary event itself, the first ever recorded in East Greenland. Yet the 10.88 mHz monochromatic seismic signal highlighted an even more globally distinctive and puzzling phenomenon. We conclude that a tsunami stabilizing into a seiche is the mechanism driving this seismic signal. This conclusion comes from four key results: (1) the near-identical frequencies (10.88 mHz versus 11.45 mHz) of the VLP signal and simulated seiche resulting from fjord geometry; (2) a fjord-transverse oscillating single-force source that fits the VLP signal's radiation pattern and its absolute amplitude using a force value theoretically expected for the oscillating water body; (3) the similar slow decay (Q~10^3) of the simulated seiche and observed VLP signal; and (4) the observed tidal modulation of the VLP seismic signal.

Even though seiches, in the presence of a persistent driving force (e.g., strong wind or storm events (*57*)), have previously been shown to have long-duration transient events or even a continuous nature (*59*), our finding provides the first evidence of fluid sloshing, at a relatively short period of 90 s (compared with seiches in open oceans), persisting for several days without requiring an external driver. In particular, we have shown how seiches in narrow, deep, parallel-sided fjords can generate distinctive long-period, ultra-long-duration seismic signals, which we would not have discovered without the combination of open data from global, high-quality, very-

broadband seismic networks (*44*, *45*). Seismic detection and accurate localization of these events heavily depend on signal amplitude, period, and station noise levels.

The Dickson Fjord event also highlights the need for networks of high-sampling rate sea-level gauge sensors to be installed in confined basins across a wide range of geographic settings to directly record such events in the near-field and in real-time (*60*). Specifically, such high-rate geophysical and hydrographic data from inside Dickson Fjord would be useful to record any further landslides and tsunamis with higher fidelity, to understand the spectral richness of the seismic signals, and to detect any background resonances of the fjord. Our seiche simulations rely on high-resolution bathymetry models, thus presenting a global challenge for accurate tsunami modeling because such data are often missing in remote areas. As our study demonstrates, multidisciplinary collaboration is beneficial to unravel these cascading events and their unusual signals, and to map, rapidly assess, and mitigate associated destructive landslide-tsunamis.

References

1. S. L. Gariano, F. Guzzetti, Landslides in a changing climate. *Earth-Sci. Rev.* 162, 227–252 (2016). doi:10.1016/j.earscirev.2016.08.011.
2. S. T. McColl, Paraglacial rock-slope stability. *Geomorphology* **153–154**, 1–16 (2012). doi:10.1016/j.geomorph.2012.02.015.
3. C. K. Ballantyne, P. Wilson, D. Gheorghiu, À. Rodés, Enhanced rock-slope failure following ice-sheet deglaciation: Timing and causes. *Earth Surf. Process. Landf.* **39**, 900–913 (2014). doi:10.1002/esp.3495.
4. A. I. Patton, S. L. Rathburn, D. M. Capps, Landslide response to climate change in permafrost regions. *Geomorphology* **340**, 116–128 (2019). doi:10.1016/j.geomorph.2019.04.029.
5. P. Saemundsson, C. Morino, S. J. Conway, “5.22 - Mass-Movements in Cold and Polar Climates” in *Treatise on Geomorphology (Second Edition)*, J. F. Shroder, Ed. (Academic Press, Oxford, 2022), pp. 350–370. doi: doi:10.1016/B978-0-12-818234-5.00117-6.
6. C. B. Harbitz, S. Glimsdal, F. Løvholt, V. Kveldsvik, G. K. Pedersen, A. Jensen, Rockslide tsunamis in complex fjords: From an unstable rock slope at Åkerneset to tsunami risk in western Norway. *Coast. Eng.* **88**, 101–122 (2014). doi:10.1016/j.coastaleng.2014.02.003.
7. F. Løvholt, G. Pedersen, C. B. Harbitz, S. Glimsdal, J. Kim, On the characteristics of landslide tsunamis. *Philos. Trans. R. Soc. Math. Phys. Eng. Sci.* **373**, 20140376 (2015). doi:10.1098/rsta.2014.0376.
8. V. Heller, G. Ruffini, A critical review about generic subaerial landslide-tsunami experiments and options for a needed step change. *Earth-Sci. Rev.* **242**, 104459 (2023). doi:10.1016/j.earscirev.2023.104459.
9. P. Poulain, A. L. Friant, A. Mangeney, S. Viroulet, E. Fernandez-Nieto, M. Castro Diaz, M. Peruzzetto, G. Grandjean, F. Bouchut, R. Pedreros, J.-C. Komorowski, Performance and limits of a shallow-water model for landslide-generated tsunamis: from laboratory experiments to simulations of flank collapses at Montagne Pelée (Martinique). *Geophys. J. Int.* **233**, 796–825 (2023). doi:10.1093/gji/ggac482.
10. B. Higman, D. H. Shugar, C. P. Stark, G. Ekström, M. N. Koppes, P. Lynett, A. Dufresne, P. J. Haeussler, M. Geertsema, S. Gulick, A. Mattox, J. G. Venditti, M. A. L. Walton, N. McCall, E. Mckittrick, B. MacInnes, E. L. Bilderback, H. Tang, M. J. Willis, B. Richmond, R. S. Reece, C. Larsen, B. Olson, J. Capra, A. Ayca, C. Bloom, H. Williams, D. Bonno, R. Weiss, A. Keen, V. Skanavis, M. Loso, The 2015 landslide and tsunami in Taan Fiord, Alaska. *Sci. Rep.* **8**, 12993 (2018). doi:10.1038/s41598-018-30475-w.
11. G. Lollino, A. Manconi, J. Locat, Y. Huang, M. Canals Artigas, Eds., *Engineering Geology for Society and Territory – Volume 4: Marine and Coastal Processes* (Springer International Publishing, Cham, 2014;

doi:10.1007/978-3-319-08660-6).

12. H. M. Fritz, F. Mohammed, J. Yoo, "Lituya Bay Landslide Impact Generated Mega-Tsunami 50th Anniversary" in *Tsunami Science Four Years after the 2004 Indian Ocean Tsunami: Part II: Observation and Data Analysis*, P. R. Cummins, K. Satake, L. S. L. Kong, Eds. (Birkhäuser, Basel, 2009), *Pageoph Topical Volumes*, pp. 153–175. doi: 10.1007/978-3-0346-0064-4_9.
13. M. Geertsema, B. Menounos, G. Bullard, J. L. Carrivick, J. J. Clague, C. Dai, D. Donati, G. Ekstrom, J. M. Jackson, P. Lynett, M. Pichierri, A. Pon, D. H. Shugar, D. Stead, J. Del Bel Belluz, P. Friele, I. Giesbrecht, D. Heathfield, T. Millard, S. Nasonova, A. J. Schaeffer, B. C. Ward, D. Blaney, E. Blaney, C. Brillon, C. Bunn, W. Floyd, B. Higman, K. E. Hughes, W. McInnes, K. Mukherjee, M. A. Sharp, The 28 November 2020 Landslide, Tsunami, and Outburst Flood – A Hazard Cascade Associated With Rapid Deglaciation at Elliot Creek, British Columbia, Canada. *Geophys. Res. Lett.* **49**, e2021GL096716 (2022). doi:10.1029/2021GL096716.
14. T. Dahl-Jensen, L. M. Larsen, S. A. S. Pedersen, J. Pedersen, H. F. Jepsen, G. Pedersen, T. Nielsen, A. K. Pedersen, F. Von Platen-Hallermund, W. Weng, Landslide and Tsunami 21 November 2000 in Paatuut, West Greenland. *Nat. Hazards* **31**, 277–287 (2004). doi:10.1023/B:NHAZ.0000020264.70048.95.
15. K. Svennevig, M. Keiding, N. J. Korsgaard, A. Lucas, M. Owen, M. D. Poulsen, J. Priebe, E. V. Sørensen, C. Morino, Uncovering a 70-year-old permafrost degradation induced disaster in the Arctic, the 1952 Niiortuut landslide-tsunami in central West Greenland. *Sci. Total Environ.* **859**, 160110 (2023). doi:10.1016/j.scitotenv.2022.160110.
16. K. Svennevig, R. L. Hermanns, M. Keiding, D. Binder, M. Citterio, T. Dahl-Jensen, S. Mertl, E. V. Sørensen, P. H. Voss, A large frozen debris avalanche entraining warming permafrost ground—the June 2021 Assapaat landslide, West Greenland. *Landslides* **19**, 2549–2567 (2022). doi:10.1007/s10346-022-01922-7.
17. K. Svennevig, T. Dahl-Jensen, M. Keiding, J. P. Merryman Boncori, T. B. Larsen, S. Salehi, A. Munck Solgaard, P. H. Voss, Evolution of events before and after the 17 June 2017 rock avalanche at Karrat Fjord, West Greenland – a multidisciplinary approach to detecting and locating unstable rock slopes in a remote Arctic area. *Earth Surf. Dyn.* **8**, 1021–1038 (2020). doi:10.5194/esurf-8-1021-2020.
18. P. Favreau, A. Mangeney, A. Lucas, G. Crosta, F. Bouchut, Numerical modeling of landquakes. *Geophys. Res. Lett.* **37**, L15305 (2010). doi:10.1029/2010GL043512.
19. G. Ekström, C. P. Stark, Simple Scaling of Catastrophic Landslide Dynamics. *Science* **339**, 1416–1419 (2013). doi:10.1126/science.1232887.
20. C. Hibert, G. Ekström, C. P. Stark, The relationship between bulk-mass momentum and short-period seismic radiation in catastrophic landslides. *J. Geophys. Res. Earth Surf.* **122**, 1201–1215 (2017). doi:10.1002/2016JF004027.
21. W. Chao, T. Wu, K. Ma, Y. Kuo, Y. Wu, L. Zhao, M. Chung, H. Wu, Y. Tsai, The Large Greenland Landslide of 2017: Was a Tsunami Warning Possible? *Seismol. Res. Lett.* **89**, 1335–1344 (2018). doi:10.1785/0220170160.
22. M. La Rocca, D. Galluzzo, G. Saccorotti, S. Tinti, G. B. Cimini, E. Del Pezzo, Seismic Signals Associated with Landslides and with a Tsunami at Stromboli Volcano, Italy. *Bull. Seismol. Soc. Am.* **94**, 1850–1867 (2004). doi:10.1785/012003238.
23. E. A. Kulikov, A. B. Rabinovich, R. E. Thomson, B. D. Bornhold, The landslide tsunami of November 3, 1994, Skagway Harbor, Alaska. *J. Geophys. Res. Oceans* **101**, 6609–6615 (1996). doi:10.1029/95JC03562.
24. J. M. Amundson, J. F. Clinton, M. Fahnestock, M. Truffer, M. P. Lüthi, R. J. Motyka, Observing calving-generated ocean waves with coastal broadband seismometers, Jakobshavn Isbræ, Greenland. *Ann. Glaciol.* **53**, 79–84 (2012). doi:10.3189/2012/AoG60A200.

25. A. B. Rabinovich, "Seiches and Harbor Oscillations" in *Handbook of Coastal and Ocean Engineering* (WORLD SCIENTIFIC, 2009), pp. 193–236. doi: doi:10.1142/9789812819307_0009.
26. D. E. McNamara, A. T. Ringler, C. R. Hutt, L. S. Gee, Seismically observed seiching in the Panama Canal. *J. Geophys. Res. Solid Earth* **116**, B04312, doi:10.1029/2010JB007930 (2011).
27. L. Gualtieri, G. Ekström, Broad-band seismic analysis and modeling of the 2015 Taan Fjord, Alaska landslide using Instaseis. *Geophys. J. Int.* **213**, 1912–1923 (2018). doi:10.1093/gji/ggy086.
28. A. Paris, E. A. Okal, C. Guérin, P. Heinrich, F. Schindelé, H. Hébert, Numerical Modeling of the June 17, 2017 Landslide and Tsunami Events in Karrat Fjord, West Greenland. *Pure Appl. Geophys.* **176**, 3035–3057 (2019). doi:10.1007/s00024-019-02123-5.
29. Materials and Methods are available as Supplementary Materials on Science Online.
30. R. Delannay, A. Valance, A. Mangeney, O. Roche, P. Richard, Granular and particle-laden flows: from laboratory experiments to field observations. *J. Phys. Appl. Phys.* **50**, 053001 (2017). doi:10.1088/1361-6463/50/5/053001.
31. A. Mangeney, Landslide boost from entrainment. *Nat. Geosci.* **4**, 77–78 (2011). doi:10.1038/ngeo1077.
32. A. Dufresne, G. J. Wolken, C. Hibert, E. K. Bessette-Kirton, J. A. Coe, M. Geertsema, G. Ekström, The 2016 Lamplugh rock avalanche, Alaska: deposit structures and emplacement dynamics. *Landslides* **16**, 2301–2319 (2019). doi:10.1007/s10346-019-01225-4.
33. L. Moretti, A. Mangeney, F. Walter, Y. Capdeville, T. Bodin, E. Stutzmann, A. Le Friant, Constraining landslide characteristics with Bayesian inversion of field and seismic data. *Geophys. J. Int.* **221**, 1341–1348 (2020). doi:10.1093/gji/ggaa056.
34. C. Hibert, G. Ekström, C. P. Stark, Dynamics of the Bingham Canyon Mine landslides from seismic signal analysis. *Geophys. Res. Lett.* **41**, 4535–4541 (2014). doi:10.1002/2014GL060592.
35. L. Moretti, K. Allstadt, A. Mangeney, Y. Capdeville, E. Stutzmann, F. Bouchut, Numerical modeling of the Mount Meager landslide constrained by its force history derived from seismic data. *J. Geophys. Res. Solid Earth* **120**, 2579–2599 (2015). doi:10.1002/2014JB011426.
36. M. I. Arran, A. Mangeney, J. De Rosny, M. Farin, R. Toussaint, O. Roche, Laboratory Landquakes: Insights From Experiments Into the High-Frequency Seismic Signal Generated by Geophysical Granular Flows. *J. Geophys. Res. Earth Surf.* **126**, e2021JF006172 (2021). doi:10.1029/2021JF006172.
37. L. Moretti, A. Mangeney, Y. Capdeville, E. Stutzmann, C. Huggel, D. Schneider, F. Bouchut, Numerical modeling of the Mount Steller landslide flow history and of the generated long period seismic waves. *Geophys. Res. Lett.* **39**, L16402 (2012). doi:10.1029/2012GL052511.
38. W. Boone, L. Ponsoni, G. Johnen, S. Rysgaard, New technologies and insights from a real-time monitoring system of sea ice and oceanographic conditions in Northeast Greenland (2023). doi:10.5194/egusphere-egu23-14430.
39. J. Macías, C. Escalante, M. J. Castro, Multilayer-HySEA model validation for landslide-generated tsunamis – Part 1: Rigid slides. *Nat. Hazards Earth Syst. Sci.* **21**, 775–789 (2021). doi:10.5194/nhess-21-775-2021.
40. G. Davies, F. Romano, S. Lorito, Global Dissipation Models for Simulating Tsunamis at Far-Field Coasts up to 60 hours Post-Earthquake: Multi-Site Tests in Australia. *Front. Earth Sci.* **8** (2020). doi:10.3389/feart.2020.598235.
41. D. Giles, E. Kashdan, D. M. Salmanidou, S. Guillas, F. Dias, Performance analysis of Volna-OP2 – massively parallel code for tsunami modelling. *Comput. Fluids* **209**, 104649 (2020). doi:10.1016/j.compfluid.2020.104649.
42. H. Q. Rif'atin, I. Magdalena, Seiches in a Closed Basin of Various Geometric Shape. *J. Phys. Conf. Ser.*

1245, 012061 (2019). doi:10.1088/1742-6596/1245/1/012061.

43. G. Pedersen, F. Løvholt, Documentation of a global Boussinesq solver. (2008).
44. A. T. Ringler, R. E. Anthony, R. C. Aster, C. J. Ammon, S. Arrowsmith, H. Benz, C. Ebeling, A. Frassetto, W.-Y. Kim, P. Koelemeijer, H. C. P. Lau, V. Lekić, J. P. Montagner, P. G. Richards, D. P. Schaff, M. Vallée, W. Yeck, Achievements and Prospects of Global Broadband Seismographic Networks After 30 Years of Continuous Geophysical Observations. *Rev. Geophys.* **60**, e2021RG000749 (2022). doi:10.1029/2021RG000749.
45. N. Leroy, M. Vallée, D. Zigone, B. Romanowicz, E. Stutzmann, A. Maggi, C. Pardo, J. Montagner, M. Bes de Berc, C. Broucke, S. Bonaimé, G. Roult, J. Thoré, A. Bernard, M. Le Cocq, O. Sirol, L. Rivera, J. Lévêque, M. Cara, F. Pesqueira, GEOSCOPE Network: 40 Yr of Global Broadband Seismic Data. *Seismol. Res. Lett.* **95**, 1495-1517 (2023). doi:10.1785/0220230176.
46. B. P. Lipovsky, E. M. Dunham, Vibrational modes of hydraulic fractures: Inference of fracture geometry from resonant frequencies and attenuation. *J. Geophys. Res. Solid Earth* **120**, 1080–1107 (2015). doi:10.1002/2014JB011286.
47. S. Cesca, J. Letort, H. N. T. Razafindrakoto, S. Heimann, E. Rivalta, M. P. Isken, M. Nikkhoo, L. Passarelli, G. M. Petersen, F. Cotton, T. Dahm, Drainage of a deep magma reservoir near Mayotte inferred from seismicity and deformation. *Nat. Geosci.* **13**, 87–93 (2020). doi:10.1038/s41561-019-0505-5.
48. R. Widmer, W. Zürn, Bichromatic excitation of long-period Rayleigh and air waves by the Mount Pinatubo and El Chichon volcanic eruptions. *Geophys. Res. Lett.* **19**, 765–768 (1992) doi:10.1029/92GL00685.
49. H. Kanamori, J. Mori, Harmonic excitation of mantle Rayleigh waves by the 1991 eruption of Mount Pinatubo, Philippines. *Geophys. Res. Lett.* **19**, 721–724 (1992). doi:10.1029/92GL00258.
50. A. M. Dziewonski, D. L. Anderson, Preliminary reference Earth model. *Phys. Earth Planet. Inter.* **25**, 297–356 (1981). doi:10.1016/0031-9201(81)90046-7.
51. S. Allgeyer, H. Hébert, R. Madariaga, Modelling the tsunami free oscillations in the Marquesas (French Polynesia). *Geophys. J. Int.* **19** , 1447–1459 (2013). doi:10.1093/gji/ggt064.
52. L. Gualtieri, G. Ekström, Broad-band seismic analysis and modeling of the 2015 Taan Fjord, Alaska landslide using Instaseis. *Geophys. J. Int.* **213**, 1912–1923 (2018). doi:10.1093/gji/ggy086.
53. A. Farhadzadeh, A study of Lake Erie seiche and low frequency water level fluctuations in the presence of surface ice. *Ocean Eng.* **135**, 117–136 (2017). doi:10.1016/j.oceaneng.2017.02.027.
54. L. Padman, M. R. Siegfried, H. A. Fricker, Ocean Tide Influences on the Antarctic and Greenland Ice Sheets. *Rev. Geophys.* **56**, 142–184 (2018). doi:10.1002/2016RG000546.
55. P. Weatherall, K. M. Marks, M. Jakobsson, T. Schmitt, S. Tani, J. E. Arndt, M. Rovere, D. Chayes, V. Ferrini, R. Wigley, A new digital bathymetric model of the world's oceans. *Earth Space Sci.* **2**, 331–345 (2015). doi:10.1002/2015EA000107.
56. P. Poulain, A. L. Friant, R. Pedreros, A. Mangeney, A. G. Filippini, G. Grandjean, A. Lemoine, E. D. Fernández-Nieto, M. J. C. Díaz, M. Peruzzetto, Numerical simulation of submarine landslides and generated tsunamis: application to the on-going Mayotte seismo-volcanic crisis. *Comptes Rendus Géoscience* **354**, 361–390 (2022). doi:10.5802/crgeos.138.
57. M. Bajo, I. Međugorac, G. Umgiesser, M. Orlić, Storm surge and seiche modelling in the Adriatic Sea and the impact of data assimilation. *Q. J. R. Meteorol. Soc.* **145**, 2070–2084 (2019). doi:10.1002/qj.3544.
58. M. Okihiro, R. T. Guza, Observations of Seiche Forcing and Amplification in Three Small Harbors. *J. Waterw. Port Coast. Ocean Eng.* **122**, 232–238 (1996). doi:10.1061/(ASCE)0733-950X(1996)122:5(232).
59. J. Park, J. MacMahan, W. V. Sweet, K. Kotun, Continuous seiche in bays and harbors. *Ocean Sci.* **12**, 355–368 (2016). doi:10.5194/os-12-355-2016.

60. M. Heidarzadeh, A. Muhari, A. B. Wijanarto, Insights on the Source of the 28 September 2018 Sulawesi Tsunami, Indonesia Based on Spectral Analyses and Numerical Simulations. *Pure Appl. Geophys.* **176**, 25–43 (2019). doi:10.1007/s00024-018-2065-9.
61. Sven Schippkus, Stephen Hicks, S. Glimsdal, Thomas Forbriger, W. Boone, Claudio Satriano, Thomas Lecocq, ROBelgium/VLPGreenland: Accepted version release, Zenodo (2024). doi:10.5281/zenodo.13221192.
62. W. Boone, S. Rysgaard, E. R. Frandsen, R. Develter, Flanders Marine Institute (VLIZ), Belgium, University Of Aarhus (AU), Denmark, Greenland Integrated Observatory - CTD & Atmospheric Station Dickson Fjord - 2023, MDA (2023). doi:10.14284/637.
63. C. Porter, I. Howat, M.-J. Noh, E. Husby, S. Khuvis, E. Danish, K. Tomko, J. Gardiner, A. Negrete, B. Yadav, J. Klassen, C. Kelleher, M. Cloutier, J. Bakker, J. Enos, G. Arnold, G. Bauer, P. Morin, ArcticDEM - Mosaics, Version 4.1, Harvard Dataverse (2023); 10.7910/DVN/3VDC4W.
64. D. Lague, N. Brodu, J. Leroux, Accurate 3D comparison of complex topography with terrestrial laser scanner: Application to the Rangitikei canyon (N-Z). *ISPRS J. Photogramm. Remote Sens.* **82**, 10–26 (2013). doi:10.1016/j.isprsjprs.2013.04.009.
65. K. L. Cook, M. Dietze, Short Communication: A simple workflow for robust low-cost UAV-derived change detection without ground control points. *Earth Surf. Dyn.* **7**, 1009–1017 (2019). doi:10.5194/esurf-7-1009-2019.
66. J. L. Carrivick, C. M. Boston, J. L. Sutherland, D. Pearce, H. Armstrong, A. Bjørk, K. K. Kjeldsen, J. Abermann, R. P. Oien, M. Grimes, W. H. M. James, M. W. Smith, Mass Loss of Glaciers and Ice Caps Across Greenland Since the Little Ice Age. *Geophys. Res. Lett.* **50**, e2023GL103950 (2023). doi:10.1029/2023GL103950.
67. C. Nuth, A. Kääb, Co-registration and bias corrections of satellite elevation data sets for quantifying glacier thickness change. *The Cryosphere* **5**, 271–290 (2011). doi:10.5194/tc-5-271-2011.
68. N. J. Korsgaard, C. Nuth, S. A. Khan, K. K. Kjeldsen, A. A. Bjørk, A. Schomacker, K. H. Kjær, Digital elevation model and orthophotographs of Greenland based on aerial photographs from 1978–1987. *Sci. Data* **3**, 160032 (2016). doi:10.1038/sdata.2016.32.
69. SDFI (Agency for Data Supply and Infrastructure), Åbent Land Grønland - Disko bugt [Vektordata, 1:50.000].
70. R. Hugonnet, R. McNabb, E. Berthier, B. Menounos, C. Nuth, L. Girod, D. Farinotti, M. Huss, I. Dussaillant, F. Brun, A. Kääb, Accelerated global glacier mass loss in the early twenty-first century. *Nature* **592**, 726–731 (2021). doi:10.1038/s41586-021-03436-z.
71. S. Rysgaard, K. Bjerge, W. Boone, E. Frandsen, M. Graversen, T. Thomas Høye, B. Jensen, G. Johnen, M. Antoni Jackowicz-Korczynski, J. Taylor Kerby, S. Kortegaard, M. Mastepanov, C. Melvad, P. Schmidt Mikkelsen, K. Mortensen, C. Nørgaard, E. Poulsen, T. Riis, L. Sørensen, T. Røjle Christensen, A mobile observatory powered by sun and wind for near real time measurements of atmospheric, glacial, terrestrial, limnic and coastal oceanic conditions in remote off-grid areas. *HardwareX* **12**, e00331 (2022). doi:10.1016/j.ohx.2022.e00331.
72. C. S. Data, retrieved from ASF DAAC on 2023, processed by ESA [accessed 2023-09-20], processed by Sentinel Hub, (2023).
73. L. G. Evers, The inaudible symphony: on the detection and source identification of atmospheric infrasound. (2008).
74. Jelle Assink, jdassink/beamforming: v1.0.0, version beamforming, Zenodo (2023). doi: 10.5281/ZENODO.10260260.

75. R. Waxler, C. H. Hetzer, J. D. Assink, P. Blom, A two-dimensional effective sound speed parabolic equation model for infrasound propagation with ground topography. *J. Acoust. Soc. Am.* **152**, 3659–3669 (2022) doi:10.1121/10.0016558.
76. R. Waxler, C. Hetzer, J. Assink, D. Velea, chetzer-ncpa/ncpaprop-release: NCPAprop v2.1.0, version v2.1.0, Zenodo (2021). doi:10.5281/ZENODO.5562712.
77. P. Blom, Modeling infrasonic propagation through a spherical atmospheric layer—Analysis of the stratospheric pair. *J. Acoust. Soc. Am.* **145**, 2198–2208, (2019). doi:10.1121/1.5096855.
78. E. E. Brodsky, E. Gordeev, H. Kanamori, Landslide basal friction as measured by seismic waves. *Geophys. Res. Lett.* **30**, 2236 (2003). doi:10.1029/2003GL018485.
79. K. Allstadt, Extracting source characteristics and dynamics of the August 2010 Mount Meager landslide from broadband seismograms. *J. Geophys. Res. Earth Surf.* **118**, 1472–1490 (2013) doi:10.1002/jgrf.20110.
80. C. Hibert, C. P. Stark, G. Ekström, Dynamics of the Oso-Steelhead landslide from broadband seismic analysis. *Nat. Hazards Earth Syst. Sci.* **15**, 1265–1273 (2015). doi:10.5194/nhess-15-1265-2015.
81. L. Toney, K. E. Allstadt, lsforce: A Python-Based Single-Force Seismic Inversion Framework for Massive Landslides. *Seismol. Res. Lett.* **92**, 2610–2626 (2021). doi:10.1785/0220210004.
82. G. Ekström, A global model of Love and Rayleigh surface wave dispersion and anisotropy, 25-250 s. *Geophys. J. Int.* **187**, 1668–1686 (2011). doi:10.1111/j.1365-246X.2011.05225.x.
83. B. L. N. Kennett, E. R. Engdahl, iasp91 velocity model. *EarthScope Earth Model Collaboration* (1991). doi:10.17611/DP/9991809.
84. F. Løvholt, G. K. Pedersen, S. Glimsdal, Coupling of dispersive tsunami propagation and shallow water coastal response. *Open Oceanogr. J.,* **4**, 71-82 (2010). doi:10.2174/1874252101004010071.
85. F. Løvholt, G. Pedersen, G. Gisler, Oceanic propagation of a potential tsunami from the La Palma Island. *J. Geophys. Res. Oceans* **113**, C09026 (2008). doi:10.1029/2007JC004603.
86. V. V. Titov, C. E. Synolakis, Numerical Modeling of Tidal Wave Runup. *J. Waterw. Port Coast. Ocean Eng.* **124**, 157–171 (1998). doi:10.1061/(ASCE)0733-950X(1998)124:4(157).
87. F. Løvholt, S. Glimsdal, P. Lynett, G. Pedersen, Simulating tsunami propagation in fjords with long-wave models. *Nat. Hazards Earth Syst. Sci.* **15**, 657–669 (2015) doi:10.5194/nhess-15-657-2015.
88. F. Løvholt, S. Glimsdal, C. B. Harbitz, On the landslide tsunami uncertainty and hazard. *Landslides* **17**, 2301–2315 (2020). doi:10.1007/s10346-020-01429-z.
89. J. Kim, "Finite volume methods for tsunamis generated by submarine landslides" thesis, Univ. Washington, Washington (2014). http://hdl.handle.net/1773/25374.
90. E. D. Fernández-Nieto, F. Bouchut, D. Bresch, M. J. Castro Díaz, A. Mangeney, A new Savage–Hutter type model for submarine avalanches and generated tsunami. *J. Comput. Phys.* **227**, 7720–7754 (2008). doi:10.1016/j.jcp.2008.04.039.
91. O. Pouliquen, Y. Forterre, Friction law for dense granular flows: application to the motion of a mass down a rough inclined plane. *J. Fluid Mech.* **453**, 133–151 (2002). doi:10.1017/S0022112001006796.
92. M. Brunet, L. Moretti, A. Le Friant, A. Mangeney, E. D. Fernández Nieto, F. Bouchut, Numerical simulation of the 30–45 ka debris avalanche flow of Montagne Pelée volcano, Martinique: from volcano flank collapse to submarine emplacement. *Nat. Hazards* **87**, 1189–1222 (2017). doi:10.1007/s11069-017-2815-5.
93. A. Le Friant, G. Boudon, C. Deplus, B. Villemant, Large-scale flank collapse events during the activity of Montagne Pelée, Martinique, Lesser Antilles. *J. Geophys. Res. Solid Earth* **108**, 2055 (2003). doi:10.1029/2001JB001624.

94. J. T. Kirby, S. T. Grilli, J. Horrillo, P. L.-F. Liu, D. Nicolsky, S. Abadie, B. Ataie-Ashtiani, M. J. Castro, L. Clous, C. Escalante, I. Fine, J. M. González-Vida, F. Løvholt, P. Lynett, G. Ma, J. Macías, S. Ortega, F. Shi, S. Yavari-Ramshe, C. Zhang, Validation and inter-comparison of models for landslide tsunami generation. *Ocean Model.* **170**, 101943 (2022) doi:10.1016/j.ocemod.2021.101943.
95. T. Esposti Ongaro, M. de' Michieli Vitturi, M. Cerminara, A. Fornaciai, L. Nannipieri, M. Favalli, B. Calusi, J. Macías, M. J. Castro, S. Ortega, J. M. González-Vida, C. Escalante, Modeling Tsunamis Generated by Submarine Landslides at Stromboli Volcano (Aeolian Islands, Italy): A Numerical Benchmark Study. *Front. Earth Sci.* **9** (2021). doi: 10.3389/feart.2021.628652.
96. Alaska Earthquake Center, Univ. of Alaska Fairbanks, Alaska Geophysical Network, International Federation of Digital Seismograph Networks (1987). doi:10.7914/SN/AK.
97. Alfred Wegener Institute For Polar And Marine Research (AWI), AW – AWI Network Antarctica, Deutsches GeoForschungsZentrum GFZ (1993). doi:10.14470/NJ617293.
98. Frank Vernon, ANZA Regional Network, International Federation of Digital Seismograph Networks (1982). doi:10.7914/SN/AZ.
99. Royal Observatory of Belgium, Belgian Seismic Network, International Federation of Digital Seismograph Networks (1985). doi:10.7914/SN/BE.
100. Northern California Earthquake Data Center, Berkeley Digital Seismic Network (BDSN), Northern California Earthquake Data Center (2014). doi:10.7932/BDSN.
101. Colorado Geological Survey, Colorado Geological Survey Seismic Network, International Federation of Digital Seismograph Networks (2016). doi:10.7914/SN/C0.
102. Universidad de Chile, Red Sismologica Nacional, International Federation of Digital Seismograph Networks (2012). doi:10.7914/SN/C1.
103. Swiss Seismological Service (SED) At ETH Zurich, National Seismic Networks of Switzerland (1983). doi:10.12686/SED/NETWORKS/CH.
104. California Institute of Technology and United States Geological Survey Pasadena, Southern California Seismic Network, International Federation of Digital Seismograph Networks (1926). doi:10.7914/SN/CI.
105. University of South Carolina, South Carolina Seismic Network, International Federation of Digital Seismograph Networks (1987). doi:10.7914/SN/CO.
106. Albuquerque Seismological Laboratory (ASL)/USGS, *Caribbean USGS Network* (International Federation of Digital Seismograph Networks, 2006. doi:10.7914/SN/CU.
107. GFZ German Research Centre For Geosciences, Institut Des Sciences De L'Univers-Centre National De La Recherche CNRS-INSU, IPOC Seismic Network, Integrated Plate boundary Observatory Chile - IPOC (2006). doi:10.14470/PK615318.
108. RESIF, RESIF-RLBP French Broad-band network, RESIF-RAP strong motion network and other seismic stations in metropolitan France, RESIF - Réseau Sismologique et géodésique Français (1995). doi:10.15778/RESIF.FR.
109. Institut De Physique Du Globe De Paris (IPGP), Ecole Et Observatoire Des Sciences De La Terre De Strasbourg (EOST), *GEOSCOPE, French Global Network of Broad Band Seismic Stations* (Institut de physique du globe de Paris (IPGP), Université de Paris, 1982; http://geoscope.ipgp.fr/networks/detail/G/). doi:10.18715/GEOSCOPE.G.
110. GEOFON Data Centre, GEOFON Seismic Network, Deutsches GeoForschungsZentrum GFZ (1993). doi:10.14470/TR560404.
111. Federal Institute for Geosciences and Natural Resources, German Regional Seismic Network (GRSN) (1976). doi:10.25928/MBX6-HR74.

112. Albuquerque Seismological Laboratory (ASL)/USGS, US Geological Survey Networks, International Federation of Digital Seismograph Networks (1980). doi:10.7914/SN/GS.
113. University of Genoa, Regional Seismic Network of North Western Italy, International Federation of Digital Seismograph Networks (1967). doi:10.7914/SN/GU.
114. Albuquerque Seismological Laboratory (ASL)/USGS, New China Digital Seismograph Network, International Federation of Digital Seismograph Networks (1992). doi:10.7914/SN/IC.
115. Scripps Institution of Oceanography, Global Seismograph Network - IRIS/IDA, International Federation of Digital Seismograph Networks (1986). doi:10.7914/SN/II.
116. Black Forest Observatory (BFO), Black Forest Observatory Data, GFZ Data Services (1971). doi:10.5880/BFO.
117. Albuquerque Seismological Laboratory/USGS, Global Seismograph Network (GSN - IRIS/USGS), International Federation of Digital Seismograph Networks (2014). doi:10.7914/SN/IU.
118. Istituto Nazionale di Geofisica e Vulcanologia (INGV), Rete Sismica Nazionale (RSN). , approx. 27 GB per day of new waveform data, approx. 415 active seismic stations, the archive totals to more than 600 distinct seismic stations (2005). doi:10.13127/SD/X0FXNH7QFY.
119. Albuquerque Seismological Laboratory (ASL)/USGS, Intermountain West Seismic Network, International Federation of Digital Seismograph Networks (2003). doi:10.7914/SN/IW.
120. Central Asian Institute for Applied Geosciences, Central Asian Seismic Network of CAIAG, International Federation of Digital Seismograph Networks (2008). doi:10.7914/SN/KC.
121. Lamont Doherty Earth Observatory (LDEO), Columbia University, Lamont-Doherty Cooperative Seismographic Network, International Federation of Digital Seismograph Networks (1970). doi:10.7914/SN/LD.
122. Instituto Dom Luiz (IDL) - Faculdade de Ciências da Universidade de Lisboa, Instituto Dom Luiz (IDL) - Faculdade de Ciencias Universidade de Lisboa, International Federation of Digital Seismograph Networks (2003). doi:10.7914/SN/LX.
123. Department of Meteorology and Hydrology - National Earthquake Data Center, Myanmar National Seismic Network, International Federation of Digital Seismograph Networks (2016). doi:10.7914/SN/MM.
124. MedNet Project Partner Institutions, Mediterranean Very Broadband Seismographic Network (MedNet). , approx. 1.1 GB/day of new data, approx. 25 active seismic broadband stations, 35 distinct seismic broadband stations (1990). doi:10.13127/SD/FBBBTDTD6Q.
125. Albuquerque Seismological Laboratory/USGS, Central and Eastern US Network, International Federation of Digital Seismograph Networks (2013). doi:10.7914/SN/N4.
126. KNMI, Caribbean Netherlands Seismic Network. , 1 GB/day (2006). doi:10.21944/DFFA7A3F-7E3A-3B33-A436-516A01B6AF3F.
127. USGS Menlo Park, USGS Northern California Seismic Network, International Federation of Digital Seismograph Networks (1966). doi:10.7914/SN/NC.
128. Utrecht University (UU Netherlands), NARS, International Federation of Digital Seismograph Networks (1983). doi:10.7914/SN/NR.
129. Instituto Nicaraguense de Estudios Territoriales (INETER), Nicaraguan Seismic Network, International Federation of Digital Seismograph Networks (1975). doi:10.7914/SN/NU.
130. GNS Science, GeoNet Aotearoa New Zealand Seismic Digital Waveform Dataset, GNS Science (2021). doi:10.21420/G19Y-9D40.
131. Rutgers University, Ocean Observatories Initiative, International Federation of Digital Seismograph Networks (2013). doi:10.7914/SN/OO.

132. Instituto Português do Mar e da Atmosfera, I.P., Portuguese National Seismic Network, International Federation of Digital Seismograph Networks (2006). doi:10.7914/SN/PM.
133. Frank Vernon, Piñon Flats Observatory Array, International Federation of Digital Seismograph Networks (2014). doi:10.7914/SN/PY.
134. Regional Integrated Multi-Hazard Early Warning System (RIMES Thailand), Regional Integrated Multi-Hazard Early Warning System, International Federation of Digital Seismograph Networks (2008). doi:10.7914/SN/RM.
135. Ruhr University Bochum, RuhrNet - Seismic Network of the Ruhr-University Bochum, Federal Institute for Geosciences and Natural Resources (BGR, Germany) (2007). doi:10.7914/SN/RN.
136. UC Santa Barbara, UC Santa Barbara Engineering Seismology Network, International Federation of Digital Seismograph Networks (1989). doi:10.7914/SN/SB.
137. Multiple Operators, International Geodynamics and Earth Tide Service, International Federation of Digital Seismograph Networks (1997). doi:10.7914/SN/SG.
138. Slovenian Environment Agency, Seismic Network of the Republic of Slovenia, International Federation of Digital Seismograph Networks (1990). doi:10.7914/SN/SL.
139. University of Leipzig, SXNET Saxon Seismic Network, International Federation of Digital Seismograph Networks (2001). doi:10.7914/SN/SX.
140. Institut fuer Geowissenschaften, Friedrich-Schiller-Universitaet Jena, Thüringer Seismologisches Netz, International Federation of Digital Seismograph Networks (2009). doi:10.7914/SN/TH.
141. Institute of Earth Sciences, Academia Sinica, Taiwan, Broadband Array in Taiwan for Seismology, International Federation of Digital Seismograph Networks (1996). doi:10.7914/SN/TW.
142. Swedish National Seismic Network, Swedish National Seismic Network, Uppsala University (1904). doi:10.18159/SNSN.
143. Albuquerque Seismological Laboratory (ASL)/USGS, United States National Seismic Network, International Federation of Digital Seismograph Networks (1990). doi:10.7914/SN/US.
144. Institut De Physique Du Globe De Paris (IPGP), *GNSS, Seismic Broadband and Strong Motion Permanent Networks in West Indies* (Institut de physique du globe de Paris (IPGP), Université de Paris, 2008; http://volobsis.ipgp.fr/networks/detail/WI/). doi:10.18715/antilles.WI.
145. San Fernando Royal Naval Observatory (ROA), Universidad Complutense De Madrid (UCM), Helmholtz-Zentrum Potsdam Deutsches GeoForschungsZentrum (GFZ), P. Universidade De Évora (UEVORA, M. Institute Scientifique Of Rabat (ISRABAT, The Western Mediterranean BB seismic Network, Deutsches GeoForschungsZentrum GFZ (1996); 10.14470/JZ581150.
146. Idaho Geological Survey, Idaho Seismic Network, International Federation of Digital Seismograph Networks (2022). doi:10.7914/SN/WW.
147. University of Utah, Yellowstone National Park Seismograph Network, International Federation of Digital Seismograph Networks (1983). doi:10.7914/SN/WY.
148. C. A. Dalton, G. Ekström, Global models of surface wave attenuation. *J. Geophys. Res. Solid Earth* **111**, 2005JB003997 (2006). doi:10.1029/2005JB003997.
149. W. Zürn, P. A. Rydelek, Revisiting the Phasor-Walkout method for detailed investigation of harmonic signals in time series. *Surv. Geophys.* **15**, 409–431 (1994). doi:10.1007/BF00666000.
150. L. Krischer, T. Megies, R. Barsch, M. Beyreuther, T. Lecocq, C. Caudron, J. Wassermann, ObsPy: a bridge for seismology into the scientific Python ecosystem. *Comput. Sci. Discov.* **8**, 014003 (2015). doi:10.1088/1749-4699/8/1/014003.
151. M. Beyreuther, R. Barsch, L. Krischer, T. Megies, Y. Behr, J. Wassermann, ObsPy: A Python Toolbox for

Seismology. *Seismol. Res. Lett.* **81**, 530–533, doi:10.1785/gssrl.81.3.530 (2010).

152. G. G. Sorrells, A Preliminary Investigation into the Relationship between Long-Period Seismic Noise and Local Fluctuations in the Atmospheric Pressure Field. *Geophys. J. R. Astron. Soc.* **26**, 71–82 (2010). doi:10.1111/j.1365-246X.1971.tb03383.x.
153. R. Beauduin, P. Lognonné, J. P. Montagner, S. Cacho, J. F. Karczewski, M. Morand, The effects of the atmospheric pressure changes on seismic signals or how to improve the quality of a station. *Bull. Seismol. Soc. Am.* **86**, 1760–1769 (1996) doi:10.1785/BSSA0860061760.
154. A. C. B. Alejandro, A. T. Ringler, D. C. Wilson, R. E. Anthony, S. V. Moore, Towards understanding relationships between atmospheric pressure variations and long-period horizontal seismic data: a case study. *Geophys. J. Int.* **223**, 676–691 (2020). doi:10.1093/gji/ggaa340.
155. P. W. Rodgers, The response of the horizontal pendulum seismometer to Rayleigh and Love waves, tilt, and free oscillations of the earth. *Bull. Seismol. Soc. Am.* **58**, 1385–1406 (1968). doi:10.1785/BSSA0580051385.
156. A. B. Baggeroer, W. A. Kuperman, H. Schmidt, Matched field processing: Source localization in correlated noise as an optimum parameter estimation problem. *J. Acoust. Soc. Am.* **83**, 571–587 (1988). doi:10.1121/1.396151.
157. S. Rost, C. Thomas, Array Seismology: Methods and Applications. *Rev. Geophys.* **40**, 2-1-2–27 (2002). doi:10.1029/2000RG000100.
158. L. Li, J. Tan, B. Schwarz, F. Staněk, N. Poiata, P. Shi, L. Diekmann, L. Eisner, D. Gajewski, Recent Advances and Challenges of Waveform-Based Seismic Location Methods at Multiple Scales. *Rev. Geophys.* **58**, e2019RG000667 (2020). doi:10.1029/2019RG000667.
159. E. Ruigrok, S. Gibbons, K. Wapenaar, Cross-correlation beamforming. *J. Seismol.* **21**, 495–508 (2017). doi:10.1007/s10950-016-9612-6.
160. M. E. Pasyanos, T. G. Masters, G. Laske, Z. Ma, LITHO1.0: An updated crust and lithospheric model of the Earth. *J. Geophys. Res. Solid Earth* **119**, 2153–2173 (2014). doi:10.1002/2013JB010626.
161. J. A. Sethian, Fast Marching Methods. *SIAM Rev.* **41**, 199–235 (1999). doi:10.1137/S0036144598347059.
162. M. Gal, A. M. Reading, N. Rawlinson, V. Schulte-Pelkum, Matched Field Processing of Three-Component Seismic Array Data Applied to Rayleigh and Love Microseisms. *J. Geophys. Res. Solid Earth* **123**, 6871–6889 (2018). doi:10.1029/2018JB015526.
163. M. C. A. White, H. Fang, N. Nakata, Y. Ben-Zion, PyKonal: A Python Package for Solving the Eikonal Equation in Spherical and Cartesian Coordinates Using the Fast Marching Method. *Seismol. Res. Lett.* **91**, 2378–2389 (2020). doi:10.1785/0220190318.
164. Z. Xu, T. D. Mikesell, Estimation of Resolution and Covariance of Ambient Seismic Source Distributions: Full Waveform Inversion and Matched Field Processing. *J. Geophys. Res. Solid Earth* **127**, e2022JB024374 (2022). doi:10.1029/2022JB024374.
165. S. Schippkus, C. Hadziioannou, Matched field processing accounting for complex Earth structure: method and review. *Geophys. J. Int.* **231**, 1268–1282 (2022). doi:10.1093/gji/ggac240.
166. S. Schippkus, schipp/fast_beamforming: 2023-09-04 first release, version v1, Zenodo (2023); 10.5281/ZENODO.8315028.
167. A. R. Hutko, M. Bahavar, C. Trabant, R. T. Weekly, M. V. Fossen, T. Ahern, Data Products at the IRIS-DMC: Growth and Usage. *Seismol. Res. Lett.* **88**, 892–903 (2017). doi:10.1785/0220160190.
168. M. Van Driel, L. Krischer, S. C. Stähler, K. Hosseini, T. Nissen-Meyer, Instaseis: instant global seismograms based on a broadband waveform database. *Solid Earth* **6**, 701–717 (2015). doi:10.5194/se-6-701-2015.

169. T. Nissen-Meyer, M. Van Driel, S. C. Stähler, K. Hosseini, S. Hempel, L. Auer, A. Colombi, A. Fournier, AxiSEM: broadband 3-D seismic wavefields in axisymmetric media. *Solid Earth* **5**, 425–445 (2014). doi:10.5194/se-5-425-2014.
170. J. Christmann, V. Helm, S. A. Khan, T. Kleiner, R. Müller, M. Morlighem, N. Neckel, M. Rückamp, D. Steinhage, O. Zeising, A. Humbert, Elastic deformation plays a non-negligible role in Greenland's outlet glacier flow. *Commun. Earth Environ.* **2**, 1–12 (2021). doi:10.1038/s43247-021-00296-3.
171. W. Bertiger, Y. Bar-Sever, A. Dorsey, B. Haines, N. Harvey, D. Hemberger, M. Heflin, W. Lu, M. Miller, A. W. Moore, D. Murphy, P. Ries, L. Romans, A. Sibois, A. Sibthorpe, B. Szilagyi, M. Vallisneri, P. Willis, GipsyX/RTGx, a new tool set for space geodetic operations and research. *Adv. Space Res.* **66**, 469–489 (2020). doi:10.1016/j.asr.2020.04.015.
172. J. Boehm, B. Werl, H. Schuh, Troposphere mapping functions for GPS and very long baseline interferometry from European Centre for Medium-Range Weather Forecasts operational analysis data. *J. Geophys. Res. Solid Earth* **111**, B02406 (2006). doi:10.1029/2005JB003629.
173. Z. Altamimi, P. Rebischung, L. Métivier, X. Collilieux, ITRF2014: A new release of the International Terrestrial Reference Frame modeling nonlinear station motions. *J. Geophys. Res. Solid Earth* **121**, 6109–6131 (2016). doi:10.1002/2016JB013098.
174. O. Hungr, S. Leroueil, L. Picarelli, The Varnes classification of landslide types, an update. *Landslides* **11**, 167–194 (2014). doi:10.1007/s10346-013-0436-y.
175. Mikkelsen, P.S., "Field report from the travel to Northeast Greenland 2023" (North-East Greenland Compagny Nanok); https://www.xsirius.dk/ (2023).
176. J. Obu, S. Westermann, A. Bartsch, N. Berdnikov, H. H. Christiansen, A. Dashtseren, R. Delaloye, B. Elberling, B. Etzelmüller, A. Kholodov, A. Khomutov, A. Kääb, M. O. Leibman, A. G. Lewkowicz, S. K. Panda, V. Romanovsky, R. G. Way, A. Westergaard-Nielsen, T. Wu, J. Yamkhin, D. Zou, Northern Hemisphere permafrost map based on TTOP modelling for 2000–2016 at 1 km2 scale. *Earth-Sci. Rev.* **193**, 299–316 (2019). doi:10.1016/j.earscirev.2019.04.023.
177. E. W. Willcox, J. Bendtsen, J. Mortensen, C. Mohn, M. Lemes, T. Juul-Pedersen, J. Holding, E. F. Møller, M. K. Sejr, M. -S. Seidenkrantz, S. Rysgaard, An Updated View of the Water Masses on the Northeast Greenland Shelf and Their Link to the Laptev Sea and Lena River. *J. Geophys. Res. Oceans* **128**, e2022JC019052 (2023). doi:10.1029/2022JC019052.
178. N. Henriksen, A. K. Higgins, F. Kalsbeek, T. C. R. Pulvertaft, Greenland from Archaean to Quaternary. Descriptive text to the Geological map of Greenland, 1: 2 500 000. *Geol. Greenl. Surv. Bull.* **185**, 2–93 (2000).
179. J. C. Escher, M. Smith, Geological Map of Greenland, l: 500,000 sheet 11, Kong Oscar Fjord: Copenhagen: Geological Survey of Denmark & Greenland. (2001).
180. P. V. Glob, M. Degerbøl, Eskimo settlements in Kempe fjord and King Oscar fjord. Treaarsexpeditionen til Christian X's Land 1931-34. *Medd. Gronl.*, , 102 (1935).
181. J. F. Jensen, M. Hardenberg, Arkæologisk berejsning af området mellem Kong Oscar Fjord og Kejser Franz Joseph Fjord Nordøstgrønland. (2012).
182. R. V. Sailor, A. M. Dziewonski, Measurements and interpretation of normal mode attenuation. *Geophys. J. Int.* **53**, 559–581 (1978). doi:10.1111/j.1365-246X.1978.tb03760.x.
183. S. Heimann, M. Isken, D. Kühn, H. Sudhaus, A. Steinberg, S. Daout, S. Cesca, H. Bathke, T. Dahm, Grond : a probabilistic earthquake source inversion framework (2018). doi:10.5880/GFZ.2.1.2018.003.
184. P. Poli, Continuation of Events Detection with Global Long-Period Seismic Data: An Analysis from 2010 to 2022. *Seismol. Res. Lett.*, **95**, 1486-1494 (2023). doi:10.1785/0220230148.

Acknowledgments

We three anonymous reviewers and L. Toney for their time taken to provide excellent and constructive comments on the first version of the manuscript. We also thank B. Shiro and J. Carter for spending substantial time to improve the presentation of the manuscript. The Joint Arctic Command, the Sirius dog sled patrol of the Kingdom of Denmark, and Northeast Greenland company Nanok are thanked for their cooperation and for making photos from after the event available to us. All initial and advanced scientific discussions were held virtually through the MatterMost platform. We are grateful to AskTom SCS for hosting this service. We are also grateful to W. Zürn for many fruitful and inspiring face-to-face discussions. We thank The Danish Agency for Data Supply and Infrastructure (SDFI) for providing GNET GNSS data. Any use of trade, firm, or product names is for descriptive purposes only and does not imply endorsement by the U.S. Government.

Funding

Danish Energy Agency / DANCEA (Danish Cooperation for Environment in the Arctic) [KS]
DT-GEO [AM]
DN EnvSeis [AM, ES, SW]
Agence Nationale de la Recherche - ANR-20-CE01-0006 [CH, JM]
PROMICE [NJK]
Agence Nationale de la Recherche - ANR-10-LABX-0023 [AL]
Agence Nationale de la Recherche - ANR-18-IDEX-0001 [AL]
German Federal Ministry of Education and Research (BMBF) [SS]
Danish Ministry of the Higher Education and Science - 5229-00005b [SR]
Aage V. Jensens Foundation - 30122021 [SR, JK, AK, ER]
H2020 European Research Council - 101058129 [SJG, SG, FL, AM]
IRD New Researcher grant [KLC]
BELSPO Brain Project - B2/191/P1/GEOCAMB [RD]
Royal Society - URF\R1\180377 [PK]
F.R.S.- FNRS through the MIS CalderaSounds funding - Fondation Wiener Anspach [CC]
H2020 European Research Council - 802777-MONIFAULTS [PP]
H2020 European Research Council [ES]
MCIN/AEI/10.13039/501100011033/European Union NextGenerationEU/PRTR/ Grant PDC2022-133663-C21 [MC]
MCIN/AEI/10.13039/501100011033/ERDF A way of making Europe Grant PID2022-137637NB-C21 [MC]
Doctoral school StepUp + Agence Innovation Défense [ND]
Belspo BRAIN project - B2/191/P1/GEOCAMB [RD]
NextGenerationEU - PID2022-137637NB-C22 [EF]
H2020 European Research Council - 101001601 [AMGF]

H2020 Europen Research Council - 852992 [AG]

Horizon Europe - 101093038, 101058129, 101058518 [AG]

National Science Foundation - EAR-2121568, EAR-2225286, OAC-2139536, OAC-2311208 [AG]

NASA - 80NSSC20K0495 [AG]

NOVO Nordisk foundation grant no NNF23OC00807040 [SAK]

New Zealand MBIE via the Strategic Science Investment Fund Hazards and Risk Management programme [ODL]

European Space Agency [JM]

Author contributions

Conceptualization: KS, SPH, TL, FL, PB

Data Curation: KS, SPH, RW, NJK, AL, REA, SS, SR, WB, PHV, BL, EC, TD, RD, LGE, MK, JK, SAK, TBL

Formal Analysis: KS, SPH, TF, TL, RW, AM, CH, NJK, AL, CS, REA, SS, SR, WB, SG, FL, AM, AL, TT, PK, CE, WDH, DGC, CC, ES, PHV, FC, TD, ND, AD, LGE, MH, MK, SAK, AK, TBL, JM, LR, ER, SW, BW

Funding Acquisition: SR, WB

Investigation: KS, SPH, TF, TL, RW, AM, CH, NJK, AL, CS, REA, AM, SS, SR, WB, SJG, KLC, SG, FL, KVN, JDA, AM, AL, TT, MS, PK, CE, AC, WDH, DGC, CC, EL, ES, PHV, TD, ND, AD, LGE, GF, MH, MK, JK, SAK, AK, ODL, TBL, BL, IM, JM, LR, ER, SW, BW, MM, KV

Methodology: KS, SPH, TF, TL, RW, AM, CH, CS, REA, SS, SJG, FL, AM, PB

Projection Administration: KS, SPH, TL, KVN

Resources: TL, AL, AD, JM, BW

Software: KS, SPH, TF, TL, RW, AM, AL, CS, REA, AM, SS, SJG, FL, AM, ES, MC, DD, EF

Supervision: KS, SPH, TL

Validation: KS, SPH, TF, TL, RW, AM, CH, AL, REA, SS, WB, SJG, FL, AM, EL, ER

Visualization: KS, SPH, TF, TL, RW, AM, CH, NJK, AL, CS, REA, AM, SS, SR, WB, SJG, KLC, SG, FL, JDA, AM, AD, LGE, SAK, LR, ER

Writing (original draft): KS, SPH, TF, TL, RW, AM, CH, REA, AM, SS, SR, WB, SJG, SG, FL, LGE, AK, ER

Writing (review & editing): KS, SPH, TF, TL, RW, AM, CH, NJK, AL, CS, REA, AM, SS, SR, WB, SJG, KLC, SG, FL, KVN, JDA, AM, AL, TT, MS, RD, PK, AC, WDH, DGC, PP, EL, ES, PHV, BL, FC, RD, LGE, AMGF, GF, AG, ALK, JK, AK, ODL, BL, IM, LR, ER, SW

Competing interests

The authors declare that they have no competing interests.

Data and materials availability

We provide a publicly available Zenodo repository (*61*) that comprises materials, data, and code to allow the main findings and figures of this paper to be reproduced. Data from the Dickson Fjord sea level gauge/CTD and

meteorological station are also publicly available (*62*). All other seismic and remote sensing data come from publicly available repositories (see Materials & Methods (*29*) for each FDSN network code and corresponding citation). The Global Seismographic Network (GSN) is a cooperative scientific facility operated jointly by the National Science Foundation (NSF) and the United States Geological Survey (USGS). The NSF component is part of the NSF SAGE Facility, operated by EarthScope Consortium under Cooperative Agreement EAR-1724509.

Supplementary Materials

- Materials and Methods (Volume calculations from Digital Elevation Models [DEMs] & Structure from Motion [SfM], Glacier elevation change; In-situ measurements in the fjord; Tsunami runup mapping methodology; Infrasound analysis; Inversion of the landslide force history; Bathymetry data; Tsunami modeling; Long-period seismic analysis; GPS data)
- Supplementary texts S1 to S6.
- Supplementary figures S1 to S40.
- Supplementary tables S1 to S3.
- Supplementary movies S1 to S3.